POLITECNICO DI TORINO
Repository ISTITUZIONALE

# Performance of segmental and shotcrete linings in shallow tunnels crossing a transverse strike-slip faulting

*Original*
Performance of segmental and shotcrete linings in shallow tunnels crossing a transverse strike-slip faulting / Zaheri, M.; Ranjbarnia, M.; Dias, D.; Oreste, P.. - In: TRANSPORTATION GEOTECHNICS. - ISSN 2214-3912. - STAMPA. - 23:(2020), p. 100333. [10.1016/j.trgeo.2020.100333]

*Availability:*
This version is available at: 11583/2940952 since: 2021-11-28T17:22:00Z

*Publisher:*
Elsevier Ltd

*Published*
DOI:10.1016/j.trgeo.2020.100333

*Terms of use:*

This article is made available under terms and conditions as specified in the corresponding bibliographic description in the repository

*Publisher copyright*

(Article begins on next page)

12 October 2024

# Performance of segmental and shotcrete linings in shallow tunnels crossing a transverse strike-slip faulting

Milad Zaheri [1], Masoud Ranjbarnia [2], Daniel Dias [3, 4], Pierpaolo Oreste [5]

[1] Department of geotechnical Engineering, Faculty of civil engineering, University of Tabriz, 29 Bahman Blvd, Tabriz, Iran, Miladzaheri@tabrizu.ac.ir

[2] Department of geotechnical Engineering, Faculty of civil engineering, University of Tabriz, 29 Bahman Blvd, Tabriz, Iran, m.ranjbarnia@tabrizu.ac.ir

[3] Antea Group, Antony, France, daniel.dias@anteagroup.com

[4] Grenoble Alpes University, Laboratory 3SR, Grenoble, France, daniel.dias@3sr-grenoble.fr

[5] Department of Environmental, Land and Infrastructure Engineering, Politecnico di Torino, Corso Duca degli Abruzzi, Torino 24-10129, Italy, Pierpaolo.oreste@polito.it

Corresponding author:

Masoud Ranjbarnia

Faculty of civil engineering, University of Tabriz, 29 Bahman Blvd, Tabriz, Iran

m.ranjbarnia@tabrizu.ac.ir

Tel.: +989144022676

**Abstract**

In this paper, three-dimensional numerical modeling is performed to study the effects of strike-slip fault movement on the performance of shotcrete and segmental linings in shallow tunnels that transversely cross the fault. For this purpose, a parametric study is conducted on lining thickness, soil geo-mechanical properties, tunnel depth, and fault dip angle to assess their influence on the tunnel movements and deformation. A comparison between the segmental and the shotcrete tunnels is made to highlight their performance. The results show that the greater strike-slip fault dip angle increases the separation of the lining segments. As well, after faulting, the maximum tunnel displacement in denser soils is greater than in loose soils.

**Keywords** Tunnel; Segmental lining; Shotcrete layer; Strike-slip fault; Numerical simulation

## 1 Introduction

Shotcrete and pre-cast concrete segments are widely used as a lining system for shallow tunnels. These lining systems are designed to withstand the static and dynamic forces, such as the gravitational overburden and earthquake loads (Gomes et al. 2001; Li et al. 2018). Furthermore, they should properly respond against the fault movement if the tunnel crosses it. In fact, any instability and collapse of these tunnels may lead to traffic problems.

For a fault, the block which is positioned above the fault plane is the hanging wall. However, the foot wall is positioned below the fault plane (see Fig. 1).

Generally, fault movement types can be categorized into four groups:

- In a reverse fault (or a thrust fault), the hanging wall moves upward relative to the foot wall, and tectonic forces are compressive (Fig. 1a);
- In a normal fault, unlike the reverse fault, the tectonic forces are tensile. Therefore, the hanging wall moves downward relative to the foot wall (Fig. 1b);
- A strike-slip fault has mostly horizontal motion. In other words, the hanging wall horizontally moves relative to the foot wall (Fig. 1c); and
- An oblique fault has a component of the strike-slip fault, and a component of the dip-slip (reverse or normal) fault (Fig. 1d).

The effects of faulting in a free field (i.e. without considering the existence of above-ground and underground structures) were investigated using centrifuge physical models, and numerical methods (Lin et al. 2006; Loukidis et al. 2009; Hazeghian and Soroush 2017). The effects of faulting on some different above-ground and buried structures were addressed in some previous studies. Geotechnical works of several types were studied, like buried pipelines (Vazouras et al. 2010; Zhang et al. 2014; Zhang et al. 2016a, b; Melissianos et al. 2016; Robert et al. 2016; Ebenuwa and Tee 2019) and foundations (deep and shallow ones) with various methods (Anastasopoulos and Gazetas 2007; Anastasopoulos et al. 2008; Bransby et al. 2008a, b; Oettle and Bray 2013; Ng et al. 2014; Soomro et al. 2017). In the case of tunnels crossing a fault, some investigations have been also carried out using numerical and small-scale physical methods, as discussed in the following.

Gregor et al. (2007) numerically modeled the stability of twin tunnels crossing a transverse oblique fault by means of FLAC$^{3D}$. The results show that the fault can cause the instability of tunnels and therefore the soil mass and water can flow into the segmental tunnels. Considering the issue of reverse faulting, Lin et al. (2007) investigated a shotcrete tunnel performance using small-scale centrifuge model tests, as well as numerical simulations (2D plane strain conditions). In their parametric study, the effects of several parameters including the

properties of soil and the tunnel layer, the fault angle, and the tunnel position relative to the fault were explored. The results demonstrated that when the tunnel is located far from the fault plane, the tunnel deformation is small. A shotcrete tunnel in a dry sandy soil was modeled by Baziar et al. (2014, 2016) using small-scale centrifuge model tests. Then, they developed a 2D numerical model (plane strain conditions), and verified their results with those of centrifuge models in order to perform parametric studies, in which the effects of the properties of soil and the shotcrete, as well as the tunnel position relative to the reverse fault were evaluated. In these tests, the fault plane (crossing the tunnel section) was parallel to the tunnel axis, and only one dip angle was selected for the faulting. It was found that the soil elastic modulus has a significant effect on tunnel movements and deformations. For the case of normal faulting and reverse faulting, Kiani et al. (2016) used small-scale physical centrifuge models to explore the pre-cast concrete segmental tunnel interaction with dry sand. Two various transverse fault dip angles were selected and the tunnel deformation mechanism under faulting was analyzed. The results showed that the number of rings affected by faulting is a function of the tunnel depth and the fault dip angle. However, the effect of soil parameters was not studied due to the limitations associated with the physical tests. Wang et al. (2012), using FLAC$^{3D}$, concisely studied all types of fault movements, except the oblique fault, on the response of the flexible lining of tunnels, and they concluded that strike-slip faults can induce a higher level of damage to deep tunnels than other faults.

This paper investigates the performance of urban tunnels crossing strike-slip faults. The segmental linings performance is investigated. As the literature review showed, this type of faulting has not been sufficiently addressed and nor comprehensively studied. It is why the need arises to investigate it. Furthermore, segmental linings are compared with continuous (i.e. shotcrete) ones in this paper. For this purpose, the interaction between the lining and the surrounding soil when faulting occurs is investigated. Therefore, in addition to the parameters related to the influence of linings and faulting parameters, the tunnel depth and the soil geo-mechanical properties are also studied.

## 2 Three Dimensional Numerical Modeling Procedure

To investigate the main parameters influencing the tunnel behavior, the finite explicit difference program FLAC$^{3D}$ was employed. The adopted numerical running procedure consists of several following phases:

- **Phase 1:** Setting up the numerical model, consisting of two parts of a fault, and assigning boundary conditions and initial stresses;
- **Phase 2:** Excavating the tunnel and installing the tunnel lining (shotcrete or concrete segments); and

- **Phase 3:** Specifying velocities to the hanging wall to shift it in the fault direction, i.e. modeling the fault movement.

**Phase 1: Setting up the numerical model**

The first step of each numerical modeling is to determine of the boundary location and chose the mesh size to avoid boundary effects and to obtain accurate results. A numerical model of 112 m width (X direction), 90 m length (Y direction in the tunnel axis direction), and 25 m height (Z direction) was chosen after a parametric study. It consists of 157920 zones and 166713 grid points (Fig. 2). It should be noted that the mesh size was refined around the tunnel.

The boundary nodes were fixed in the direction perpendicular to the Y-Z plane (X= -56 m and X= 56 m) and to the X-Z plane (Y= 0 m and Y= 90 m). The base nodes of the model were fixed in the vertical direction (Zakhem and El Naggar 2019; Ziaei and Ahangari 2018) (Fig. 3). Then, the properties of soil and the lining were assigned to the model (see section 4 for more detailed information about the constitutive models).

Then, initial vertical (the gravity is taken into account), as well as horizontal stresses (by multiplying the vertical stresses by the lateral earth pressure factor ($K_0$)) were assigned to the whole model.

This numerical model consists of two parts, the hanging wall and the foot wall. These parts were connected by an interface to simulate the shearing and sliding mechanisms, and to model the fault. Interface elements are utilized to represent shear planes in which differential movements between the hanging wall and the foot wall can easily occur. If these elements are not utilized in the numerical simulations, the strain localization cannot be imposed in the fault plane and therefore the fault movement mechanism and its influence on the tunnel lining cannot be correctly modeled. The properties to be considered for the interface are including the friction angle, cohesion, dilation angle, normal and shear stiffnesses, and tensile strength (Itasca, 2005). The shearing behavior of this interface is characterized by a linear elastic perfectly plastic constitutive model (Mohr-coulomb criterion), and the same soil properties were assigned to it (e.g. the dilation angle and the friction angle). Similarly, both the normal and shear stiffnesses of the interface were chosen as equal to ten times the equivalent stiffness given by Equation (1) (Itasca, 2005).

$$\max\left[\frac{K+\frac{4}{3}G}{\Delta z_{min}}\right] \tag{1}$$

where K and G are the bulk modulus and the shear modulus, respectively, and the smallest dimension of a neighboring zone in the normal direction is $\Delta z_{min}$ (Itasca, 2005; Do et al. 2013, 2014a, b, c, d and e, 2015; Zaheri et al. 2019).

**Phase 2: Excavating the tunnel and installing the tunnel lining**

A single circular tunnel (with a diameter (D) of 5.9 m) was excavated and at the same time, the lining was installed. As shown in Fig. 4, the pre-cast concrete segments or the shotcrete layer was considered as the tunnel lining. These linings were modeled using 'liner' elements which have a linear-elastic behavior. Although the tunnel lining exhibits a nonlinear elasto-plastic behavior even in the case of a small fault movement, in FLAC$^{3D}$ only a linear elastic behavior can be assigned to the tunnel lining (Itasca, 2005; Do et al. 2013, 2014a, b, c, d and e, 2015; Baghban Golpasand et al. 2019). This can induce a difference when comparing numerical results with the observed behavior. To overcome this limit and consider the ultimate limit state in the tunnel lining, two criteria are proposed to control if instability is occurring. These criteria are presented in the following study.

When a liner is created, FLAC$^{3D}$ automatically attaches this liner to the adjacent medium via an interface. The behavior of this interface is controlled by two springs (in the normal and tangential direction to the liner surface) and strength parameters (such as tensile strength, friction angle and cohesion) (Itasca, 2005). In other words, the normal behavior of this interface controlled by the normal stiffness and the tensile strength. The shear behavior is cohesive and frictional and is controlled by the shear coupling spring properties (shear stiffness, cohesive strength, and friction angle) and the normal stress acting on (Itasca, 2005). Thus, this interface can slide in the tangent plane and be separated from soil in the normal direction. In the case of segmental tunnel, as shown in Fig. 5, each node of a liner has two links: one is attached to the soil mass and the other one connects the segments together.

The liner-zone interface stiffnesses (normal stiffness ($K_n$) and shear stiffness ($K_s$)) were determined by a good rule of thumb (recommended by Itasca 2005), in which these values are one hundred times the equivalent stiffness of Equation (1). The reason for multiplying the equivalent stiffness of Equation (1) by 100 is the fact that this equation is applied only to a planar surface subjected to normal penetration and if the surface is curved (such as the lining of tunnel) the apparent stiffness should be increased by a factor of 100 (Itasca 2005).

As described by Do et al. 2013, 2014a, b, c, d and e, 2015, for the interaction between segments, connection in the tangential and axial directions (of the tunnel) were simulated using a node to node connection

which included six degrees of freedom. For each of these degrees, one spring was assigned (three translational components in the x, y, and z directions and three rotational components around these mentioned directions).

In this study, as shown in Figs. 6 and 7, the connection of segments in the tangential direction (ring) was represented by a set composed of a radial spring ($K_R$), an axial stiffness ($K_A$), and a rotational spring ($K_\theta$) (Do et al. 2013, 2014a, b, c, d and e, 2015), and in the axial direction (between adjacent rings) by a set composed of a radial spring ($K_{RR}$), an axial stiffness ($K_{AR}$), and a rotational spring ($K_{\theta R}$) (Do et al. 2014c, d, 2015).

A bi-linear relation was assumed for the behavior of these stiffnesses, and their values were computed by the method of Do et al. 2013. However, in the tangential direction (between the segments in a ring), the attachment conditions of the two rotational components around the x and z directions and the translational component in the y direction (in the local coordinate system) were assumed to be rigid in all of the investigated cases. On the other hand, in the axial direction (between the rings), the attachment conditions were set to be rigid for the two rotational components around the y and z directions. The above-mentioned directions were in the local system. According to the geometric state of the fault plane relative to the tunnel axis, these assumptions have no effects on the results.

It was assumed that the position of the segment joints in the odd and even rings are different. In other words, each ring position, compared to the previous one was rotated 30°. The position of joints and the segment joint parameters are summarized in Table 1 (see also Fig. 4a) and Table 2.

**Table 1.** Position of the segment joints (measured clockwise from the tunnel crown)

| Ring order | Joint location |
|---|---|
| Odd rings | 0°, 60°, 120°, 180°, 240°, 300° |
| Even rings | 30°, 90°, 150°, 210°, 247°, 330° |

**Table 2.** Parameters of the segment joints

| Parameter | Symbol | Unit | Value |
|---|---|---|---|
| Rotational stiffness of the joint | $k_\theta$ | MN m/rad/m | 100[a] |
| Maximum bending moment at the segment joint | $M_{yield}$ | MN.m/m | 0.15[a] |
| Axial stiffness of the joint | $k_A$ | MN/m | 500[a] |
| Maximum axial forces at the segment joint | $T_c$ | MN/m | 0.06 |
| Radial stiffness of the joint | $k_R$ | MN/m | 1050[a] |

| | | | |
|---|---|---|---|
| Maximum shear forces at the segment joint | $S_{yield}$ | MN/m | 0.27 |

Note: [a] Assumed by Do et al. 2014c.

**Phase 3: Simulation of the fault movement**

To model the fault movement, a velocity was assigned to the hanging wall in a given number of calculation steps. If the applied maximum displacement and the velocity are denoted by d and V, respectively, then the number of steps (N) will be equal to $N = \frac{d}{V}$ ) (Itasca, 2005). The given velocity was assigned in the X-direction, as shown in Fig. 2. In this study, the number of steps was set to 17000, which implied a velocity of $V=1.47 * 10^{-4}$ (m/calculation step) to reach a maximal movement of 2.5 m in the fault direction. It should be mentioned that the large strain mode was used for this step, i.e. the nodal coordinates were updated at each calculation step. As stated before, although the tunnel lining exhibits a nonlinear elasto-plastic behavior even in the case of a small fault movement, in $FLAC^{3D}$, only a linear elastic behavior can be assigned to the tunnel lining (Itasca, 2005; Do et al. 2013, 2014a, b, c, d and e, 2015; Miranda et al. 2014; Moeinossadat and Ahangari 2019).

**3 Verification of the numerical model**

A numerical model should be calibrated with the results of analytical and/or physical models. However, the case of a strike-slip fault offset influence on tunnels has not been conducted by the aforementioned methods. Therefore, in the absence of data for this fault type, a comparison of the results was made for the case of a dip-slip faulting. The validity of the numerical modeling procedures was carried out by comparing them with those of centrifuge physical modeling by Kiani (2016) and Kiani et al. (2016).

In the aforementioned studies, the influence of a dip-slip faulting (reverse and normal faulting) on a segmental tunnel was studied using centrifuge physical tests (Kiani, 2016; Kiani et al. 2016). In these tests, a dry sandy soil was poured in a rigid box in layers that were compacted to reach a relative density of 60%. After reaching the desired value of soil thickness, the segmental tunnel (constructed using cement pipes) was placed in the soil layer. Then, the filling of the rigid box was continued until it reached the ground level (Kiani, 2016; Kiani et al. 2016). In the following step, the model was subjected to a fault displacement applied by a hydraulic jack to the moving part of the rigid box in the fault direction.

The properties of soil and the tunnel used in the considered physical model are summarized in Table 3 (the tunnel diameter and the segment thickness at the prototype scale were respectively equal to 5.9 m and 0.45

m). Table 4 presents the maximum tunnel displacements and the affected length of the tunnel due to the reverse and normal faulting at the prototype scale.

**Table 3.** Properties of the soil and of the tunnel in the centrifuge test level (Kiani, 2016; Kiani et al. 2016)

| Parameter | Unit | Value |
|---|---|---|
| Elastic modulus of soil | MPa | 20 |
| Friction angle of soil | - | 37 |
| Soil density | $kg/m^3$ | 1630 |
| Poisson's ratio of soil | - | 0.3 |
| Cohesion of soil | $kN/m^2$ | 0 |
| Segment density | $kg/m^3$ | 2600 |
| Poisson's ratio of segment | - | 0.28 |
| Elastic modulus of segment | GPa | 20 |

**Table 4.** Comparison of results obtained by the centrifuge physical test model and by the numerical model (Kiani, 2016; Kiani et al. 2016)

| Fault type | Fault angle | Height of overburden of soil (m) | Maximum displacement of the tunnel (m) | |
|---|---|---|---|---|
| | | | In the centrifuge physical test | In the numerical method |
| Reverse | 60˚ | 0.75D | 0.55 | 0.545 |
| Reverse | 75˚ | 0.75D | 0.256 | 0.25 |
| Normal | 60˚ | 1D | 2.50 | 2.50 |
| Normal | 75˚ | 1D | 2.50 | 2.50 |

To simulate the fault movement, in the first step, the dimensions of the numerical model were chosen 50 times greater than the physical model tests. In the next step, the elastic-perfectly plastic stress-strain constitutive model (the Mohr-Coulomb failure criteria) was assigned to the medium. Then, using the methodology discussed in the previous section, the fault movement (equal to 2.5 meters) was simulated. It should be mentioned that sensitive analyses were performed for the mesh size and the location of boundaries to obtain accurate results. For various mesh refinements, the vertical displacements of the tunnel due to the normal fault offset are shown in Fig. 8. As seen, the results are not mesh dependent and the difference between the results is small. For the dip-slip

faulting (reverse and normal faulting), the ground displacements in the experimental method were compared with the numerical ones. As an example, for both experimental and numerical models, the ground displacements after reverse (with the angle of 75° measured from the horizontal line and the overburden height of 0.75D) and normal (with the angle of 60° and the overburden height of 1D) faulting are shown in Fig. 9 (D is the tunnel diameter). As observed, the results of these methods are very similar and in good agreement. Furthermore, a comparison is made for the maximum displacements of the tunnel. The maximum displacements of the tunnel in the above-mentioned methods are summarized in Table 4. As seen, the results of the numerical method are very close to those obtained in the centrifuge physical model. Thus, the finite difference method can be considered as validated and in the next sections, a parametric study will be performed.

## 4 The parametric study and input data

A parametric study was conducted to evaluate the effects of multiple parameters on the displacement of the tunnel (tunnel movement), the development of the soil plastic strains, and the deformation of the tunnel cross-section due to the fault movement. According to Table 5, combining of three tunnel depths and two soil types, i.e. dense or loose states (to which were assigned three values of friction angle, one value of elastic modulus ($E_s$)), and one value of density), 18 cases were obtained.

**Table 5.** Properties of the basic cases used in the parametric study

| Parameter | Symbol | Unit | Value |
|---|---|---|---|
| Soil type | - | - | Loose soil, Dense soil |
| Elastic modulus of soil | $E_s$ | MPa | 15, 40 |
| Peak friction angle of soil | $\emptyset_{peak}$ | ° | (24, 28, 30), (35, 36, 38) |
| Peak dilation angle of soil | $\Psi_{Peak}$ | ° | 5, 6, 8 |
| Soil density | $\rho_s$ | kg/m$^3$ | 1500, 1800 |
| Tunnel depth | H | m | 10, 12, 14 |

For the dense soil, the Mohr-Coulomb strain-hardening/softening constitutive model was chosen, in which the soil mechanical properties were the function of the deviatoric plastic strains. The position of a stress point on this failure envelope is controlled by a non-associated flow rule for shear failure and an associated rule for tension failure (Itasca, 2005). It was assumed that the soil friction component was decreases linearly with the

increase of the deviatoric plastic strains up to 10% (Fig. 10) (Atkinson, 2007). Also, it was assumed that the relation between the friction angle ($\phi$) and the dilation angle ($\Psi$) was governed by Equation (2). However, for the loose granular soil, the linear elastic with perfect plasticity (Mohr-Coulomb failure criteria) was considered. In this state, the soil dilation angle is equal to zero.

$$\Psi = \phi - 30° \quad (2)$$

Since the analyses were time-consuming, a reference case was selected by choosing one case from each soil type accompanied by one tunnel depth. For each type of lining system, this reference case could be combined with three fault dip angles (measured from the horizontal line), as well as three tunnel lining thicknesses to give 27 cases (summing up 18 cases and 9 cases) (Table 6). The properties of soil and the lining in the reference case are summarized in Table 7. It should be noted that for preliminary tunnel design, it is sufficient to consider the mean values of the parameters. Thus, spatial variability of soil properties is not considered here (Li and Low 2010; Ali et al. 2017; Kroetz et al. 2018; Titi et al. 2018).

**Table 6.** The values of tunnel lining thickness and fault dip angle in the parametric study

| Parameter | Symbol | Unit | Value |
|---|---|---|---|
| Thickness of the tunnel lining | $t_l$ | m | 0.35, 0.40, 0.45 |
| Fault dip angle | $\alpha$ | ° | 60, 75, 90 |

**Table 7.** Soil and lining properties in the reference case

| Parameter | Symbol | Unit | Dense soil | Loose soil |
|---|---|---|---|---|
| Elastic modulus of soil | $E_s$ | MPa | 40 | 15 |
| Peak friction angle of soil | $\emptyset_{peak}$ | ° | 35 | 24 |
| Peak dilation angle of soil | $\Psi_{Peak}$ | ° | 5 | 0 |
| Residual friction angle of soil | $\emptyset_{residual}$ | ° | 30 | 24 |
| Soil density | $\rho_s$ | kg/m$^3$ | 1800 | 1500 |
| Poisson's ratio of soil | $v_s$ | - | 0.30 | 0.30 |
| Cohesion of soil | c | kN/m$^2$ | 0 | 0 |
| Tunnel burial depth | H | m | 12 | 12 |
| Width of tunnel lining | w | m | 1.5 | 1.5 |

| | | | | |
|---|---|---|---|---|
| Tunnel lining density | $\rho_l$ | kg/m$^3$ | 2500 | 2500 |
| Elastic modulus of tunnel lining | $E_l$ | GPa | 35 | 35 |
| Thickness of tunnel lining | $t_l$ | m | 0.35 | 0.35 |
| Poisson's ratio of tunnel lining | $v_l$ | - | 0.28 | 0.28 |
| Fault dip angle | $\alpha$ | ° | 60 | 60 |

## 5 Results and discussion

This section deals with tunnel movements after strike-slip faulting. Fig. 11 shows the final state of the model after 2.5 m fault movement. In this condition, the tunnel cross section is sheared and the segments might be separated. Unlike normal or reverse faulting, the strike-slip fault offset does not impose a great ground surface upward or downward movement, and hence, it is not discussed here.

### 5.1 Effects of the tunnel layer thickness

In the case of the segmental tunnel, the lining thickness ($t_l$) was considered as 0.35 m, 0.40 m, and 0.45 m while in the shotcrete tunnels, it was 0.25 m, 0.30 m, and 0.35 m.

Horizontal displacements of the tunnel left side (point L in Fig. 3) at different stages of faulting are depicted in Fig. 12 for the reference case of the dense soil ("d" indicates the fault displacement value). As observed, for fault displacements lower than 1 m, no separation of segments between rings occurs, which means that segmental tunnels can sustain the fault movements. Also, increasing the fault offset leads to increase of the separation between adjacent rings (shear stress exceeds the shear strength between adjacent rings). For example, when the fault movement is equal to 1.5 meters, the separation between adjacent rings is equal to 0.1 meters and a 2 m fault movement leads to about 0.3 m of separation between adjacent rings. As well, increasing the fault offset magnitude leads the shotcrete and segmental tunnels to sustain more displacement. This is in agreement with previous works such as those conducted by Baziar et al. (2014, 2016), in which the impact of a reverse faulting on a shotcrete tunnel was investigated.

Also, when the fault offset is small, the induced bending stresses are not considerable. As the fault movement increases, the curvature of the segmental tunnel increases. This means that the tunnel layer experiences more bending stresses. In this figure, the zero value of the horizontal distance from the fault refers to the intersection of the fault plane and the bedrock (point O in Fig. 2b).

Fig. 13 represents the left side displacements of the tunnel after full faulting for both the segmental and shotcrete tunnels. As seen, increasing the thickness of segments causes the increase of the absorbed energy in the joints. Because the stiffness and strength between segments of adjacent rings are constant, the shear displacement between adjacent rings slightly increases. Also, it seems that the lining thickness for these two lining types has no significant effect.

After the fault offset, independently of the segmental thickness, three rings are more influenced and separated. The length of the tunnel affected by faulting ($L_e$) is defined as the distance between the first and the last separation of segments of adjacent rings in the axial direction of the tunnel (Fig. 14). Hence, the maximum separation between adjacent rings (see Fig. 13a) and the $L_e$ value are equal to 0.55 m and 0.76D, respectively. The segmental tunnel deformation, as well as the separation between adjacent rings, in the reference case of the dense soil are shown in Fig. 14. It implies that increasing the tunnel layer thickness only increases the project cost and has not a significant effect during the faulting.

The contours of plastic strains in the fault plane of the hanging wall, in the case of segmental and shotcrete tunnels are depicted in Figs. 15 and 16, respectively. For segmental tunnels, a semi-elliptical shape can be seen and plastic strains in this area are very low. However, out of this area, the plastic strains increase. On the other hand, in the case of the shotcrete tunnel, increasing the layer thickness causes the plastic strains to be intensified.

### 5.2. Effects of the mechanical properties of soil

Loose and dense granular soils with different mechanical properties are studied. Comparing the results in Fig. 17, the state of soil (dense or loose) can influence the tunnel maximum displacement (see also Table 8). As seen, in both shotcrete and segmental tunnels, the maximum displacement of the tunnel in the denser soils is greater than in loose soils. For example, the maximum displacement of the segmental or the shotcrete tunnel in the dense granular soil, when the peak friction angle ($\emptyset_{peak}$) is equal to 35°, is about 1.10 times greater compared to the loose one with 30° friction angle. In loose soils, a part of the forces resulting from faulting causes the soil to become denser. However, this displacement is not affected by altering the soil mechanical properties, either in the dense or loose soils, and it seems that only the soil state influences the stated parameter. In other words, in the case of either shotcrete or segmental tunnels, when the peak friction angle of the soil is equal to 24°, the displacement is more or less the same as the one obtained for a friction angle of 30°. Similar results were observed in the experimental studies performed by Baziar et al. (2014, 2016). They showed that when a reverse fault crosses a tunnel, the soil stiffness has a great influence on the shotcrete tunnel displacements. On the other hand, these

results showed that the soil friction angle slightly influences the tunnel displacement. It can be also seen that no separation between adjacent rings occurred in the tunnels with the lower mechanical properties (see also Fig. 18). On the other hand, regardless of the dense soil mechanical properties, the separation occurs among three rings. Also, the $L_e$ parameter and the maximum separation value between adjacent rings are equal to 0.76D and 0.55 m, respectively.

The contours of plastic strains shown in Fig. 19 reveal that these plastic strains tend to be spread out over a narrower area in the loose soil. No separation between the adjacent rings and the compression of particles (due to low soil elastic modulus value ($E_s$)) can be the reasons for this phenomenon.

**Table 8.** Effect of the soil geomechanical properties on the maximum tunnel displacement after the faulting

| $\emptyset_{peak}$ (°) | $\Psi_{Peak}$ (°) | $\rho_s$ (kg/m$^3$) | $E_s$ (MPa) | Maximum displacement of segmental tunnel (m) | Maximum displacement of shotcrete tunnel (m) |
|---|---|---|---|---|---|
| 35 | 5 | 1800 | 40 | 2.22 | 2.33 |
| 36 | 6 | 1800 | 40 | 2.21 | 2.33 |
| 38 | 8 | 1800 | 40 | 2.20 | 2.33 |
| 24 | - | 1500 | 15 | 2.05 | 2.18 |
| 28 | - | 1500 | 15 | 2.02 | 2.14 |
| 30 | - | 1500 | 15 | 2.01 | 2.13 |

### 5.3 Effects of the tunnel depth

This section demonstrates that the tunnel depth is one of the important factors that can have a significant influence on its performance. In fact, choosing an appropriate tunnel depth in the design phase can permit to prevent instabilities. The investigation of the deformed rings shows that three, three and four rings are subjected to the separation corresponding to the tunnel depths (H) of 10 m, 12 m, and 14 m, respectively. The maximum separation of the rings equals 0.71 m, 0.55 m, and 0.78 m, respectively (Fig. 20). It implies that there is not any specific trend in the maximum separation against the value of the overburden, and should be studied in any practical cases. However, for the case in which the tunnel depth is equal to 14 m, the values of separation and the length of the tunnel affected by the faulting are the greatest. It should be noted that, in the numerical simulations, changing the segmental tunnel depth leads the hanging wall tunnel area to be altered. This point must be considered when designing tunnels. Also, increasing the shotcrete tunnel depth leads to a slight increase of the

tunnel movements, however, the tunnel displacements are similar to the ones of Fig. 13b, and thus these figures are not depicted (see Table 9).

According to Fig. 21, in the case of both segmental and shotcrete tunnels, the contours of the soil plastic strains tend to be enhanced when the tunnel depth is greater. In other words, the size of the semi elliptical shape decreases when the tunnel is located closer to the ground surface.

**Table 9.** Effect of the tunnel depth on the maximum shotcrete tunnel displacements after the faulting

| Tunnel depth (H) (m) | Tunnel maximum displacement (m) |
|---|---|
| 10 | 2.36 |
| 12 | 2.32 |
| 14 | 2.28 |

### 5.4 Effects of the fault dip angle

As seen in Figs. 22 and 23, in the case of the segmental tunnel, when the fault angle is equal to 60° and 75° (with respect to the horizontal line), three and two rings are subjected to the separation, respectively. Furthermore, a negligible deformation occurs in one ring when the fault dip angle is 90°. Also, it can be seen that when the fault plane is perpendicular to the segmental tunnel axis, the maximum tunnel displacement is slightly greater than for other fault angles. For the fault with the dip angle equal to 60°, to 75° and to 90°, the maximum separation between the adjacent rings in the horizontal direction is equal to 0.55 m, 1.46 m and 1.86 m, respectively. Noted that changing the fault dip angle causes the tunnel area in the hanging wall to be influenced. For example, when the fault dip angle is 90°, the fault exactly intersects the tunnel in the middle of the two adjacent rings (see Fig. 23). This point must be also considered at the design stage. As seen in Fig. 22b, the greater the fault angle, the more curvature of the shotcrete tunnel.

When the fault dip angle is equal to 60° (reference case of the dense soil), a distortion is observed in the tunnel shape, but by increasing the fault dip angle, this distortion is reduced. Also, increasing the fault angle leads to the dissipation of the semi elliptical shape i.e. more plastic zones are generated as the fault dip angle is higher (see Fig. 24a). A similar trend can be seen in the case of the shotcrete tunnel (Fig. 24a and Fig. 24b).

### 5.5 Tunnel cross section deformation

The other important issue which should be explored is the maximum tunnel deformation of the segmental tunnel. The obtained results are summarized in Table 10. The results show that

- The segmental tunnel layer thickness ($t_l$) has a negligible influence;
- The tunnel deformation is considerably affected by the soil state. The denser the soil, the greater the tunnel deformation;
- Increasing the fault dip angle (α), as well as reducing the tunnel burial depth (H) reduces the tunnel deformation.

Finally, two criteria are defined to estimate the instability of tunnel segments:

1) When the shear stress in the segment's connection is greater than the possible shear strength, as seen in all the cases, the shear stress of at least one of the adjacent rings exceeds the shear strength (Table 2), and then instability occurs;
2) When the tunnel deformation (strain) is greater than the ultimate rupture strain of concrete, which is usually equal to 0.002 (ACI, 2011; Leblais et al. 2014). Since large fault movements can impose more stress (and also strains) on the supporting system of tunnels, the lining cannot remain in the elastic state and therefore, it follows a plastic behavior (see Table 10).

**Table 10.** Deformation of the segmental tunnel in the horizontal direction after faulting

| The cases | Secondary tunnel diameter in the horizontal direction (m) | Tunnel deformation in the horizontal direction (%) |
|---|---|---|
| The reference case of the dense soil (see Table 7) | 5.30 | -10.12 |
| $t_l$= 0.40 m | 5.30 | -10.06 |
| $t_l$= 0.45 m | 5.32 | -9.79 |
| Loose soil, $\emptyset$ = 24°, $E_s$= 15 MPa | 5.85 | -0.69 |
| Loose soil, $\emptyset$ = 28°, $E_s$ = 15 MPa | 5.83 | -1.05 |
| Loose soil, $\emptyset$ = 30°, $E_s$ = 15 MPa | 5.83 | -1.17 |
| Dense soil, $\emptyset_{peak}$ = 36°, $E_s$ = 40 MPa | 5.25 | -10.97 |
| Dense soil, $\emptyset_{peak}$ = 38°, $E_s$ = 40 MPa | 5.17 | -12.35 |

| | | |
|---|---|---|
| H = 10 m | 5.43 | -7.82 |
| H = 14 m | 4.95 | -16.06 |
| α = 75° | 5.67 | -3.84 |
| α = 90° | 5.85 | -0.80 |

## 6 Conclusion

This paper presented a three-dimensional numerical study of the interaction between the tunnel lining and a strike-slip fault. For this purpose, a parametric study was conducted to investigate the influence of the soil mechanical properties, the layer thickness of the segmental and shotcrete tunnels, the tunnel burial depth, and the fault dip angle. Following main conclusions can be drawn from the present study:

- The shotcrete tunnel layer thickness has no influence on the tunnel movement after faulting. The greater thickness of the segmental tunnel causes an increase of the separation distance between adjacent segments. However, the segmental tunnel layer thickness has a negligible influence on the tunnel cross section deformation and the maximum tunnel movement;
- The tunnel with segmental liners can sustain slight fault movements, however, after some deformation, the rings cannot resist the fault offset. Then, the separation between the adjacent rings can be seen;
- The length of the tunnel affected by faulting ($L_e$) is a function of the tunnel depth and the fault dip angle. This parameter is not influenced by the tunnel layer thickness;
- Unlike dense granular soils, neither the maximum segmental tunnel movement nor the tunnel deformation is great in loose soils. Also, in loose soils, no separation between the adjacent rings occurs. In the shotcrete tunnel, a similar result can be seen about the soil mechanical effects on the tunnel movements;
- The magnitude of separation between adjacent rings in the segmental tunnel is almost the same for various friction angles of the dense soil;
- Both of the tunnel deformation and $L_e$ parameter tend to be greater when the tunnel depth is enhanced;
- It seems that there is not any specific trend in the maximum separation between adjacent rings against the value of the tunnel overburden;
- The deeper shotcrete tunnels embedded in the soil with higher mechanical properties experience larger movements after faulting compared to other cases. The lower fault angle can intensify this effect;

- A greater fault dip angle intensifies the magnitude of separation between adjacent rings, meanwhile, it induces a smaller tunnel deformation.

**References**

ACI Committee International Organization for Standardization. Building code requirements for structural concrete (ACI 318-08) and commentary; 2011: American Concrete Institute.

Ali A, Lyamin AV, Huang J, Sloan SW, Cassidy MJ. Undrained stability of a single circular tunnel in spatially variable soil subjected to surcharge loading. Computers and Geotechnics. 2017; 84:16-27. DOI: https://doi.org/10.1016/j.compgeo.2016.11.013.

Anastasopoulos I, Callerio A, Bransby M, Davies M, El Nahas A, Faccioli E, et al. Numerical analyses of fault–foundation interaction. Bulletin of earthquake engineering. 2008; 6(4):645-75. DOI: https://doi.org/10.1007/s10518-008-9078-1.

Anastasopoulos I, Gazetas G. Foundation–structure systems over a rupturing normal fault: Part II. Analysis of the Kocaeli case histories. Bulletin of Earthquake Engineering. 2007; 5(3):277-301. DOI: https://doi.org/10.1007/s10518-007-9030-9.

Atkinson J. The mechanics of soils and foundations: CRC Press; 2007.

Baghban Golpasand M-R, Do NA, Dias D. Impact of pre-existent Qanats on ground settlements due to mechanized tunneling. Transportation Geotechnics. 2019; 21:100262. DOI: https://doi.org/10.1016/j.trgeo.2019.100262.

Baziar MH, Nabizadeh A, Lee CJ, Hung WY. Centrifuge modeling of interaction between reverse faulting and tunnel. Soil Dynamics and Earthquake Engineering. 2014; 65:151-64. DOI: https://doi.org/10.1016/j.soildyn.2014.04.008.

Baziar MH, Nabizadeh A, Mehrabi R, Lee CJ, Hung WY. Evaluation of underground tunnel response to reverse fault rupture using numerical approach. Soil Dynamics and Earthquake Engineering. 2016; 83:1-17. DOI: https://doi.org/10.1016/j.soildyn.2015.11.005.

Bransby M, Davies M, El Nahas A, Nagaoka S. Centrifuge modelling of reverse fault–foundation interaction. Bulletin of Earthquake Engineering. 2008a; 6(4):607-28. DOI: https://doi.org/10.1007/s10518-008-9080-7.

Bransby M, Davies M, Nahas AE. Centrifuge modelling of normal fault–foundation interaction. Bulletin of Earthquake Engineering. 2008b; 6(4):585-605. DOI: https://doi.org/10.1007/s10518-008-9079-0.

Do N-A, Dias D, Oreste P, Djeran-Maigre I. 2D numerical investigation of segmental tunnel lining behavior. Tunnelling and Underground Space Technology. 2013; 37:115-27. DOI: https://doi.org/10.1016/j.tust.2013.03.008.

Do N-A, Dias D, Oreste P, Djeran-Maigre I. 2D numerical investigations of twin tunnel interaction. Geomech Eng, Int J. 2014a; 6(3):263-75.

Do N-A, Dias D, Oreste P, Djeran-Maigre I. 2D tunnel numerical investigation: the influence of the simplified excavation method on tunnel behaviour. Geotechnical and Geological Engineering. 2014b; 32(1):43-58. DOI: https://doi.org/10.1007/s10706-013-9690-y.

Do N-A, Dias D, Oreste P, Djeran-Maigre I. Three-dimensional numerical simulation for mechanized tunnelling in soft ground: the influence of the joint pattern. Acta Geotechnica. 2014c; 9(4):673-94. DOI: https://doi.org/10.1007/s11440-013-0279-7.

Do N-A, Dias D, Oreste P, Djeran-Maigre I. Three-dimensional numerical simulation of a mechanized twin tunnels in soft ground. Tunnelling and Underground Space Technology. 2014d; 42:40-51. DOI: https://doi.org/10.1016/j.tust.2014.02.001.

Do N-A, Dias D, Oreste P. 2D seismic numerical analysis of segmental tunnel lining behaviour. Bulletin of the New Zealand Society for Earthquake Engineering. 2014e; 47(3):206-16.

Do N-A, Dias D, Oreste P. 3D numerical investigation on the interaction between mechanized twin tunnels in soft ground. Environmental Earth Sciences. 2015; 73(5):2101-13. DOI: https://doi.org/10.1007/s12665-014-3561-6.

Ebenuwa AU, Tee KF. Reliability estimation of buried steel pipes subjected to seismic effect. Transportation Geotechnics. 2019; 20:100242. DOI: https://doi.org/10.1016/j.trgeo.2019.100242.

Eclaircy-Caudron S, Dias D, Kastner R, Miranda TF, Correia AG, Sousa L, editors. Inverse analysis on two geotechnical works: a tunnel and a cavern. In Proceedings of the 5th Int Workshop on Applications of Computational Mechanics in Geotechnical Engineering; 2007.

Gomes RC, Oliveira CS, Correia AG, editors. Seismic Response Assessment of Underground Structure Cross-Sections Using Response Spectra. International Conferences on Recent Advances in Geotechnical Earthquake Engineering and Soil Dynamics; 2001.

Gregor T, Garrod B, Young D, editors. Analyses of underground structures crossing an active fault in Coronado, California. Proceedings of the World Tunnel Congress; 2007.

Hazeghian M, Soroush A. Numerical modeling of dip-slip faulting through granular soils using DEM. Soil Dynamics and Earthquake Engineering. 2017; 97:155-71. DOI: https://doi.org/10.1016/j.soildyn.2017.03.021.

Itasca. Fast Lagrangian analysis of continua in 3-dimension (flac3d v3.1). Itasca Consulting Group; 2005.

Kiani M, Akhlaghi T, Ghalandarzadeh A. Experimental modeling of segmental shallow tunnels in alluvial affected by normal faults. Tunnelling and Underground Space Technology. 2016; 51:108-19. DOI: https://doi.org/10.1016/j.tust.2015.10.005.

Kiani M. Effects of surface fault rupture on shallow segmental soil tunnels-centrifuge modeling. Tabriz, Iran: University of Tabriz; 2016 (in Persian).

Kroetz HM, Do NA, Dias D, Beck AT. Reliability of tunnel lining design using the Hyperstatic Reaction Method. Tunnelling and Underground Space Technology. 2018; 77:59-67. DOI: https://doi.org/10.1016/j.tust.2018.03.028.

Leblais Y, Andre D, Chapeau C, Dubois P, Gigan J, Guillaume J, et al. Settlements induced by tunnelling. AFTES Recommendations. 1995.

Li H-Z, Low BK. Reliability analysis of circular tunnel under hydrostatic stress field. Computers and Geotechnics. 2010; 37(1):50-8. DOI: https://doi.org/10.1016/j.compgeo.2009.07.005.

Li Z, Ye J, Lin W, Bian X, Chen Y. Effect of Metro Excavation on Soft Clay's Displacement and Strength Behaviors Based on In-situ Tests. Environmental Vibrations and Transportation Geodynamics. Singapore: Springer Singapore; 2018. p. 775-83. DOI: https://doi.org/10.1007/978-981-10-4508-0_72.

Lin M-L, Chung C-F, Jeng F-S, Yao T-C. The deformation of overburden soil induced by thrust faulting and its impact on underground tunnels. Engineering Geology. 2007; 92(3-4):110-32. DOI: https://doi.org/10.1016/j.enggeo.2007.03.008.

Lin M-L, Chung C-F, Jeng F-S. Deformation of overburden soil induced by thrust fault slip. Engineering Geology. 2006; 88(1-2):70-89. DOI: https://doi.org/10.1016/j.enggeo.2006.08.004.

Loukidis D, Bouckovalas GD, Papadimitriou AG. Analysis of fault rupture propagation through uniform soil cover. Soil Dynamics and Earthquake Engineering. 2009; 29(11-12):1389-404. DOI: https://doi.org/10.1016/j.soildyn.2009.04.003.

Melissianos VE, Korakitis GP, Gantes CJ, Bouckovalas GD. Numerical evaluation of the effectiveness of flexible joints in buried pipelines subjected to strike-slip fault rupture. Soil Dynamics and Earthquake Engineering. 2016; 90:395-410. DOI: https://doi.org/10.1016/j.soildyn.2016.09.012.

Miranda T, Correia A, Sena-Cruz J, Costa L, Dias D. Analysis of the performance of an evolutionary computation algorithm in the identification of geomechanical parameters in underground works2014. DOI: https://doi.org/10.1201/b16955-168.

Moeinossadat SR, Ahangari K. Estimating maximum surface settlement due to EPBM tunneling by Numerical-Intelligent approach – A case study: Tehran subway line 7. Transportation Geotechnics. 2019; 18:92-102. DOI: https://doi.org/10.1016/j.trgeo.2018.11.009.

Ng CWW, Soomro MA, Hong Y. Three-dimensional centrifuge modelling of pile group responses to side-by-side twin tunnelling. Tunnelling and Underground Space Technology. 2014; 43:350-61. DOI: https://doi.org/10.1016/j.tust.2014.05.002.

Oettle NK, Bray JD. Geotechnical mitigation strategies for earthquake surface fault rupture. Journal of Geotechnical and Geoenvironmental Engineering. 2013; 139(11):1864-74. DOI: https://doi.org/10.1061/(ASCE)GT.1943-5606.0000933.

Robert D, Soga K, O'Rourke T. Pipelines subjected to fault movement in dry and unsaturated soils. International Journal of Geomechanics. 2016; 16(5):C4016001. DOI: https://doi.org/10.1061/(ASCE)GM.1943-5622.0000548.

Soomro MA, Ng CWW, Liu K, Memon NA. Pile responses to side-by-side twin tunnelling in stiff clay: Effects of different tunnel depths relative to pile. Computers and Geotechnics. 2017; 84:101-16. DOI: https://doi.org/10.1016/j.compgeo.2016.11.011.

Titi HH, Faheem A, Tabatabai H, Tutumluer E. Influence of Aggregate Base Layer Variability on Pavement Performance. Transportation Research Record. 2014; 2457(1):58-71. DOI: https://doi.org/10.3141/2457-07.

Titi HH, Tabatabai H, Faheem A, Tutumluer E, Peters JP. Spatial variability of compacted aggregate bases. Transportation Geotechnics. 2018; 17:56-65. DOI: https://doi.org/10.1016/j.trgeo.2018.06.007.

Vazouras P, Karamanos SA, Dakoulas P. Finite element analysis of buried steel pipelines under strike-slip fault displacements. Soil Dynamics and Earthquake Engineering. 2010; 30(11):1361-76. DOI: https://doi.org/10.1016/j.soildyn.2010.06.011.

Wang Z, Zhang Z, Gao B, editors. Seismic behavior of the tunnel across active fault. The 15th world conference on earthquake engineering, Lisbon, Portugal, Sept; 2012.

Zaheri M, Ranjbarnia M, Oreste P. Performance of systematic fully grouted rockbolts and shotcreted layer in circular tunnel under the hydrostatic conditions using 3D finite difference approach. Geomechanics and Geoengineering. 2019:1-14. DOI: https://doi.org/10.1080/17486025.2019.1648885.

Zakhem A-M, El Naggar H. Effect of the constitutive material model employed on predictions of the behaviour of earth pressure balance (EPB) shield-driven tunnels. Transportation Geotechnics. 2019; 21:100264. DOI: https://doi.org/10.1016/j.trgeo.2019.100264.

Zhang J, Liang Z, Han CJ. Buckling behavior analysis of buried gas pipeline under strike-slip fault displacement. Journal of Natural Gas Science and Engineering. 2014; 21:921-8. DOI: https://doi.org/10.1016/j.jngse.2014.10.028.

Zhang L, Zhao X, Yan X, Yang X. A new finite element model of buried steel pipelines crossing strike-slip faults considering equivalent boundary springs. Engineering Structures. 2016a; 123:30-44. DOI: https://doi.org/10.1016/j.engstruct.2016.05.042.

Zhang L, Zhao X, Yan X, Yang X. Elastoplastic analysis of mechanical response of buried pipelines under strike-slip faults. International Journal of Geomechanics. 2016b; 17(4):04016109. DOI: https://doi.org/10.1061/(ASCE)GM.1943-5622.0000790.

Ziaei A, Ahangari K. The effect of topography on stability of shallow tunnels case study: The diversion and conveyance tunnels of Safa Dam. Transportation Geotechnics. 2018; 14:126-35. DOI: https://doi.org/10.1016/j.trgeo.2017.12.001.

**Figure Captions**

**Fig. 1.** Fault types a) Reverse fault b) Normal fault c) strike-slip fault d) Oblique fault

**Fig. 2.** Perspective view of the numerical model and meshes a) 3D view b) Longitudinal view

**Fig. 3.** Adopted boundary conditions

**Fig. 4.** Considered scheme a) Segmental tunnel b) Shotcrete tunnel

**Fig. 5.** Segment joint scheme (Do et al. 2014c)

**Fig. 6.** $K_R$, $K_A$, $K_\theta$ stiffnesses in the radial, axial, and rotational directions of a segment joint (Do et al. 2014c)

**Fig. 7.** $K_{RR}$, $K_{AR}$, $K_{\theta R}$ stiffnesses in the radial, axial, and rotational directions between adjacent rings (Do et al. 2014c)

**Fig. 8.** Effect of mesh sizes on the tunnel deflection values (the first and second numbers in the legend of this figure represent the number of meshes in the Y and Z directions, respectively)

**Fig. 9.** Ground surface displacements in the numerical and experimental methods

**Fig. 10.** Soil friction and dilation angles versus plastic shear strains considered in the dense granular soil

**Fig. 11.** Final state of the model after the strike-slip fault movement

**Fig. 12.** The tunnel deformation at different stages of the strike-slip faulting a) Segmental tunnel b) Shotcrete tunnel

**Fig. 13.** Effect of the lining thickness on the tunnel left side displacements a) Segmental tunnel b) Shotcrete tunnel

**Fig. 14.** Plane view of the tunnel deformation after strike-slip faulting (reference case for dense soil)

**Fig. 15.** Effect of the segmental tunnel layer thickness on the deformed mesh of the fault plane

**Fig. 16.** Effect of the shotcrete tunnel layer thickness on the deformed mesh of the fault plane

**Fig. 17.** Effect of the soil mechanical properties on the tunnel left side displacements a) Segmental tunnel b) Shotcrete tunnel

**Fig. 18.** Plane view of tunnel lining deformation after strike-slip faulting (loose soil with a friction angle (∅) and an elastic modulus ($E_s$) equal to 30°, 15 MPa, respectively)

**Fig. 19.** Effect of the soil mechanical properties on the deformed mesh of the fault plane ($\phi = 24°, \varphi = 0°, \rho_s = 1500\frac{Kg}{m^3}, and\ E_s = 15\ MPa$) a) Segmental tunnel b) Shotcrete tunnel

**Fig. 20.** Effect of the segmental tunnel burial depth on the tunnel left side displacements

**Fig. 21.** Effect of the tunnel burial depth on the deformed mesh of the fault plane (tunnel depth (H) = 14 m) a) Segmental tunnel b) Shotcrete tunnel

**Fig. 22.** Effect of the fault dip angle on the tunnel left side displacements a) Segmental tunnel b) Shotcrete tunnel

**Fig. 23.** Plane view of tunnel deformation after faulting

**Fig. 24.** Effect of the fault dip angle on the deformed mesh of the fault plane (fault dip angle (α) = 90°) a) Segmental tunnel b) Shotcrete tunnel

a)

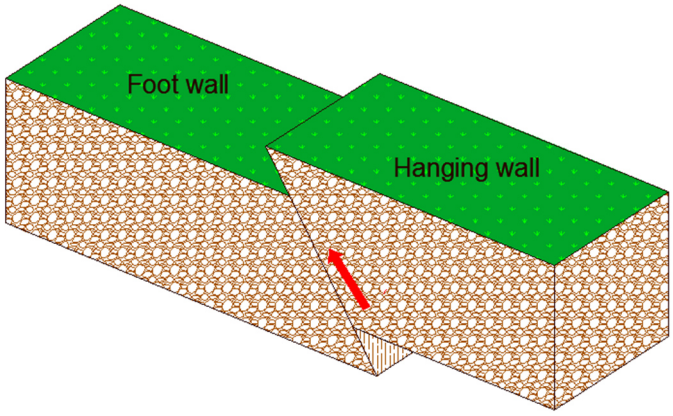
Foot wall
Hanging wall

b)

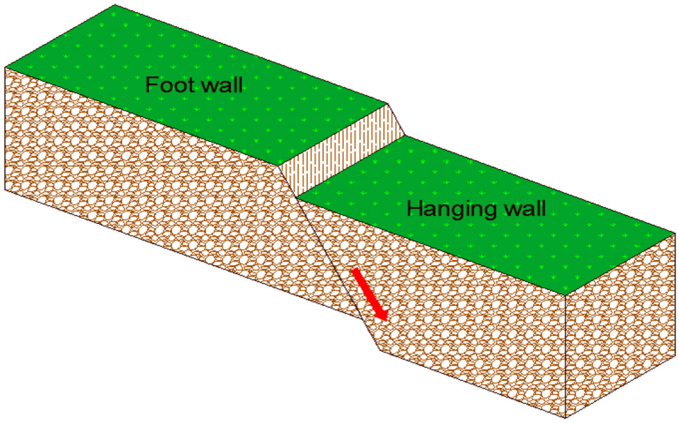
Foot wall
Hanging wall

c)

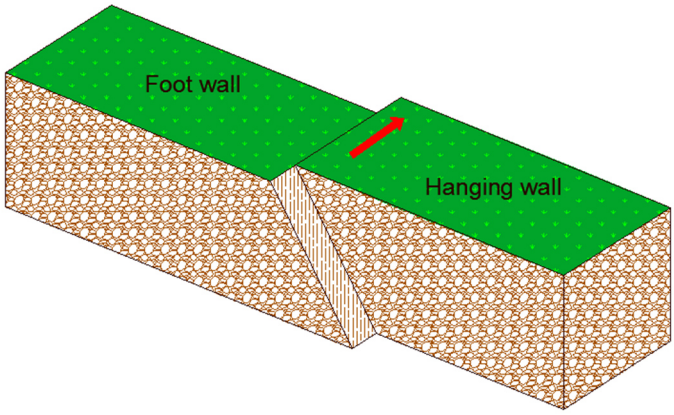
Foot wall
Hanging wall

d)

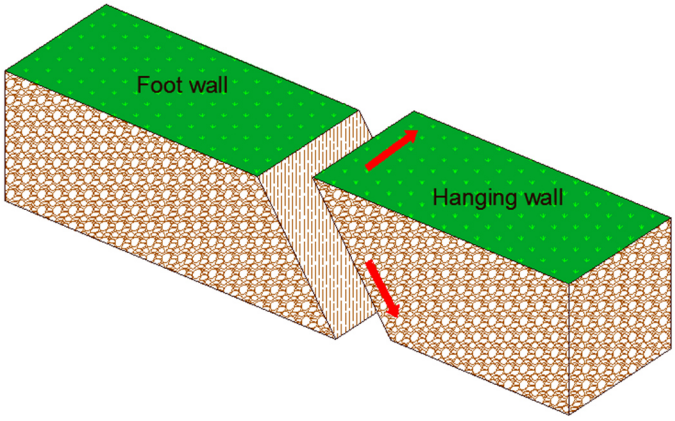


**Fig. 1**

a)

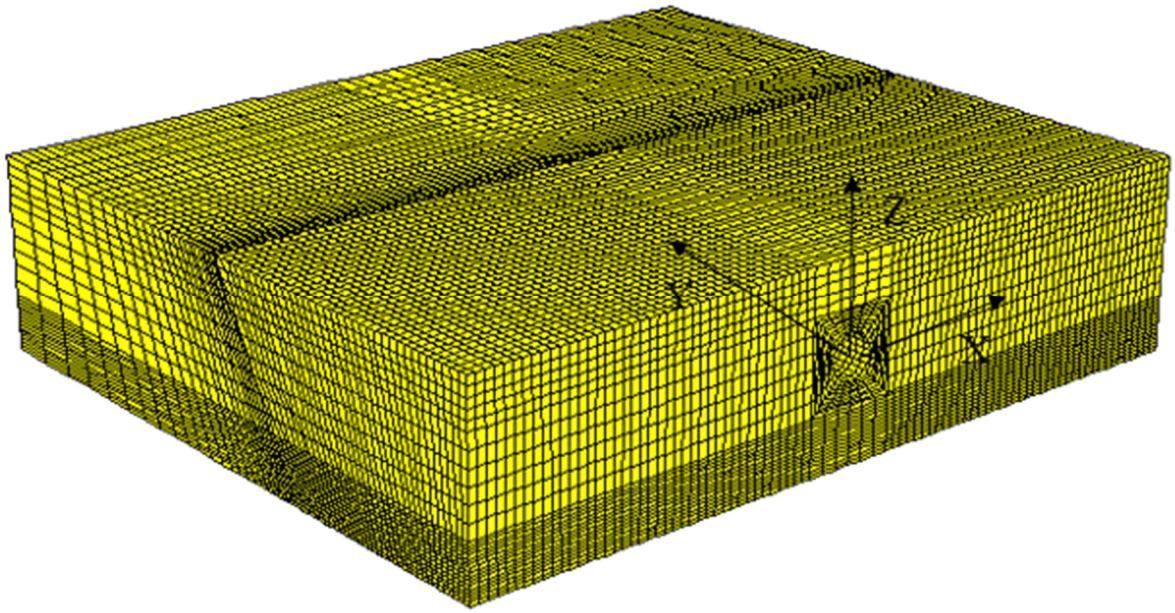


b)

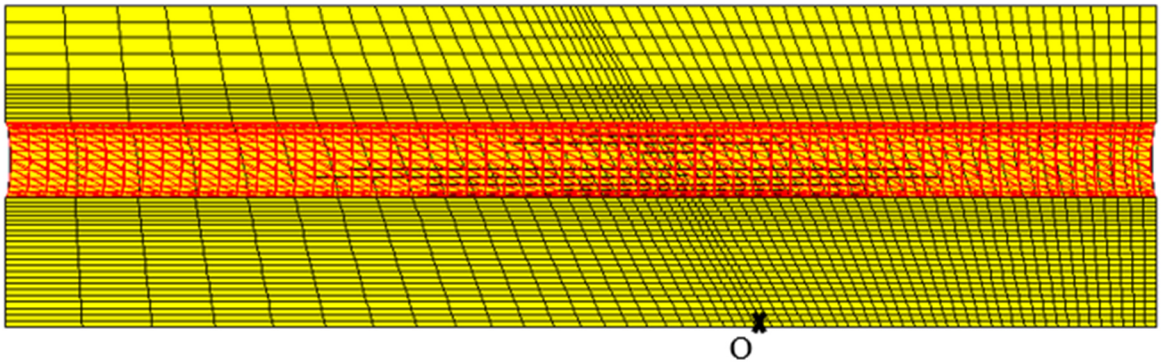


**Fig. 2**

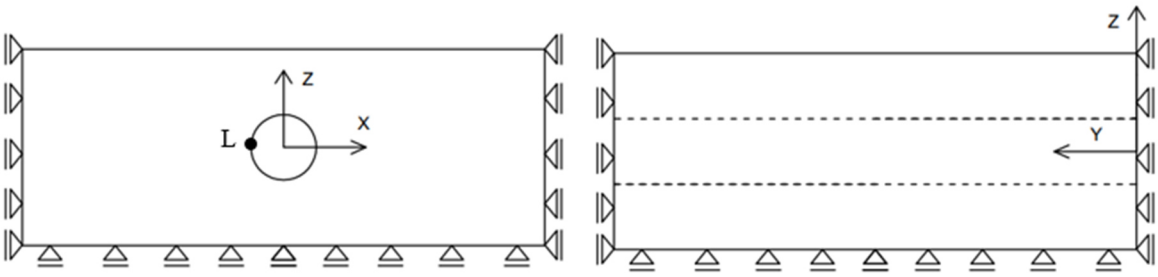


**Fig. 3**

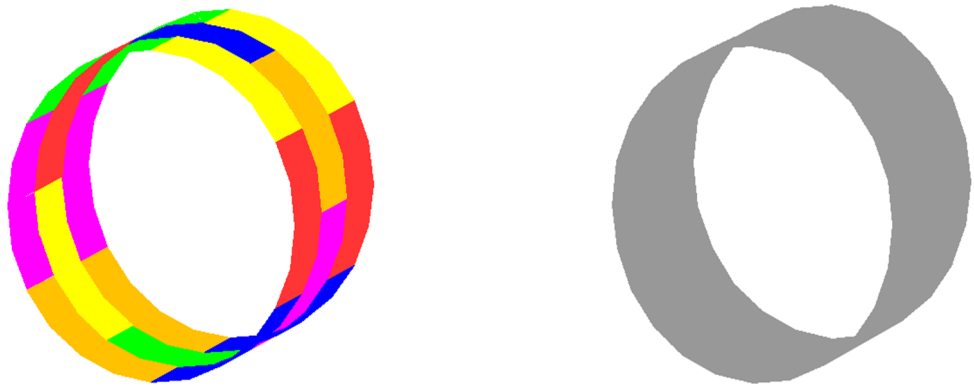

a) b)

**Fig. 4**

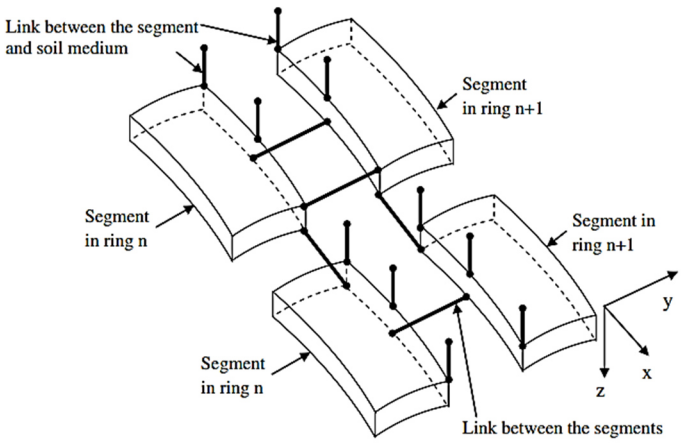


**Fig. 5**

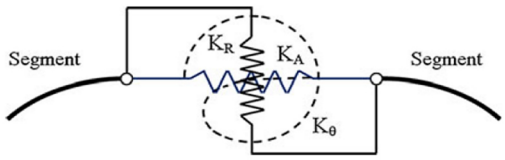


**Fig. 6**

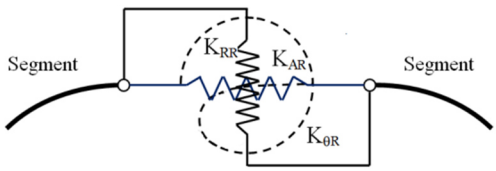


**Fig. 7**

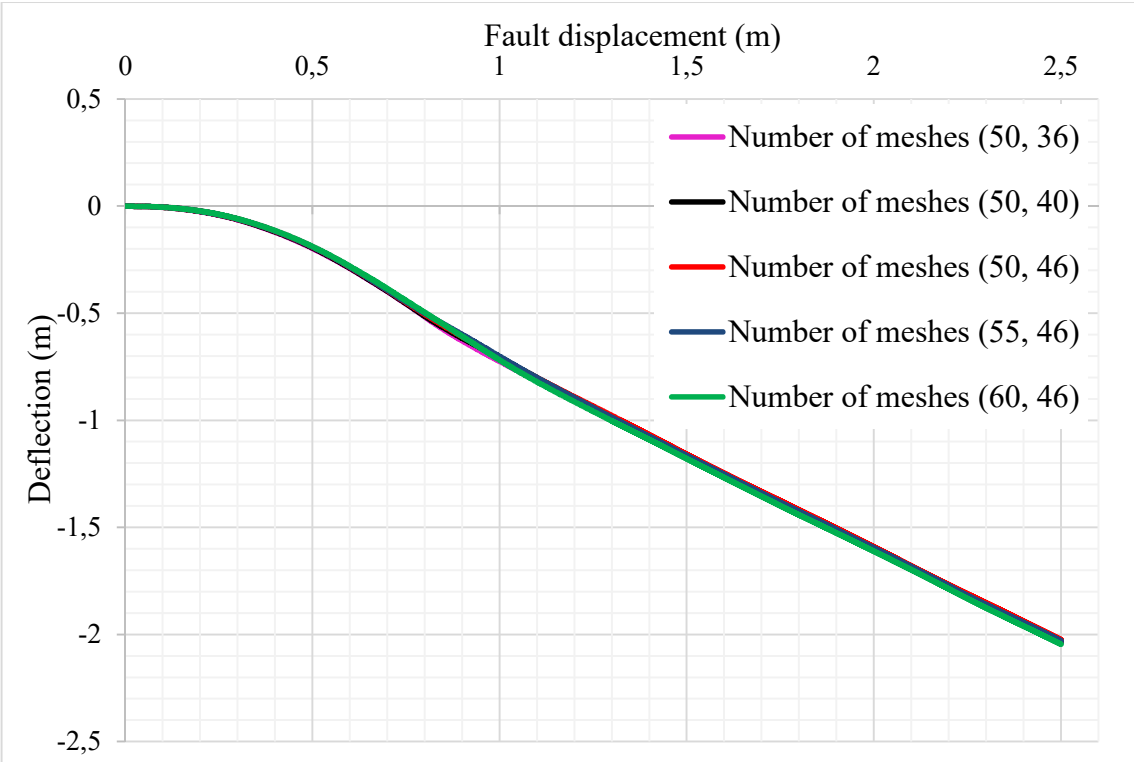
Fault displacement (m)
0
0,5
1
1,5
2
2,5
0,5
0
-0,5
-1
-1,5
-2
-2,5
Deflection (m)
Number of meshes (50, 36)
Number of meshes (50, 40)
Number of meshes (50, 46)
Number of meshes (55, 46)
Number of meshes (60, 46)

**Fig. 8**

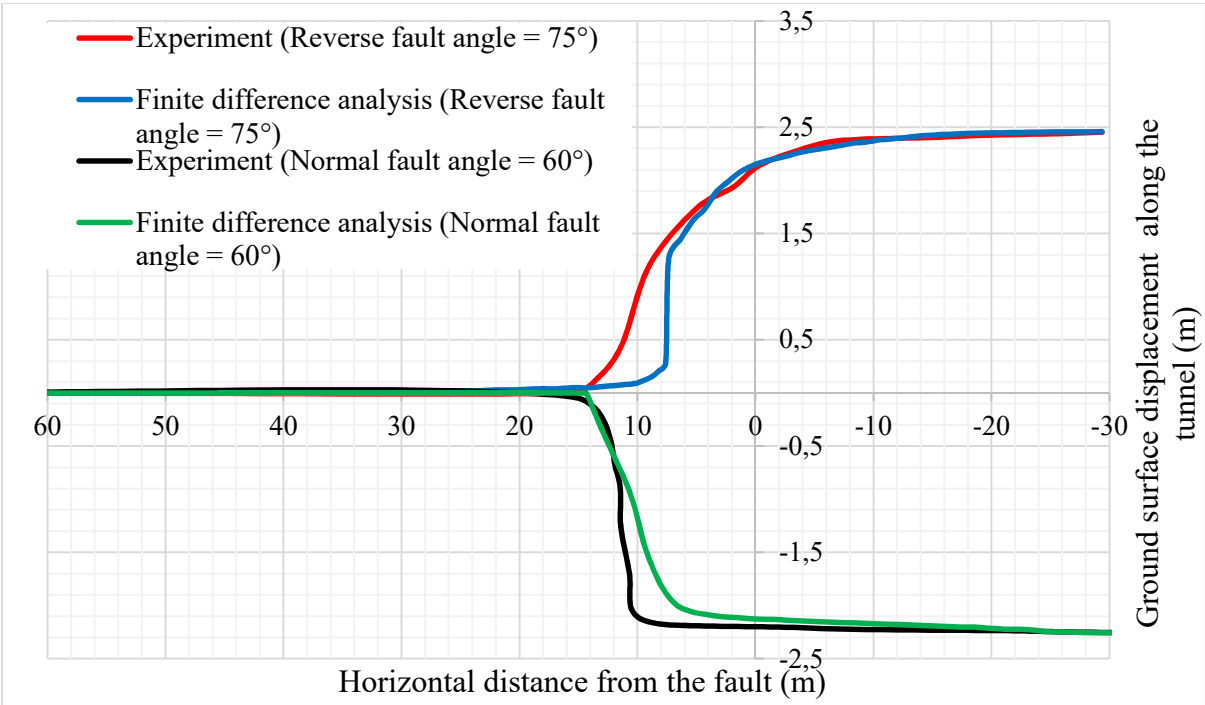
Experiment (Reverse fault angle = 75°)
Finite difference analysis (Reverse fault angle = 75°)
Experiment (Normal fault angle = 60°)
Finite difference analysis (Normal fault angle = 60°)
3,5
2,5
1,5
0,5
-0,5
-1,5
-2,5
60
50
40
30
20
10
0
-10
-20
-30
Horizontal distance from the fault (m)
Ground surface displacement along the tunnel (m)

**Fig. 9**

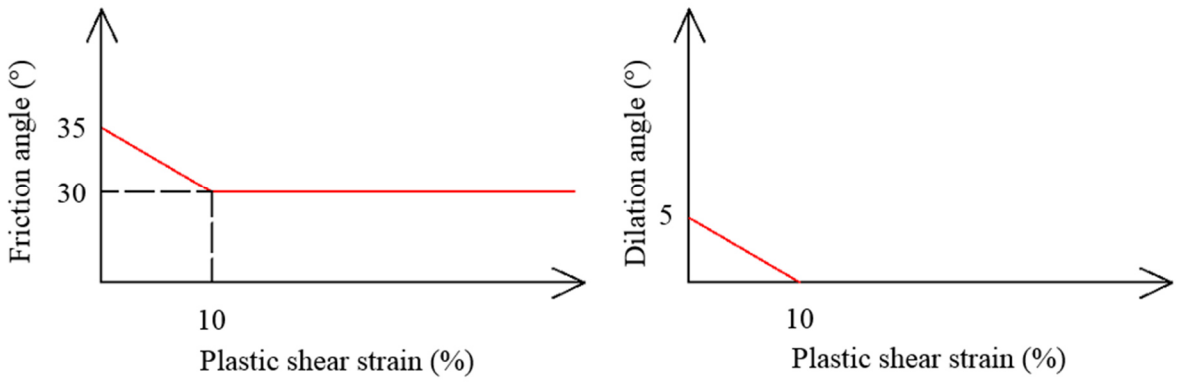
Friction angle (°)
35
30
10
Plastic shear strain (%)
Dilation angle (°)
5
10
Plastic shear strain (%)

**Fig. 10**

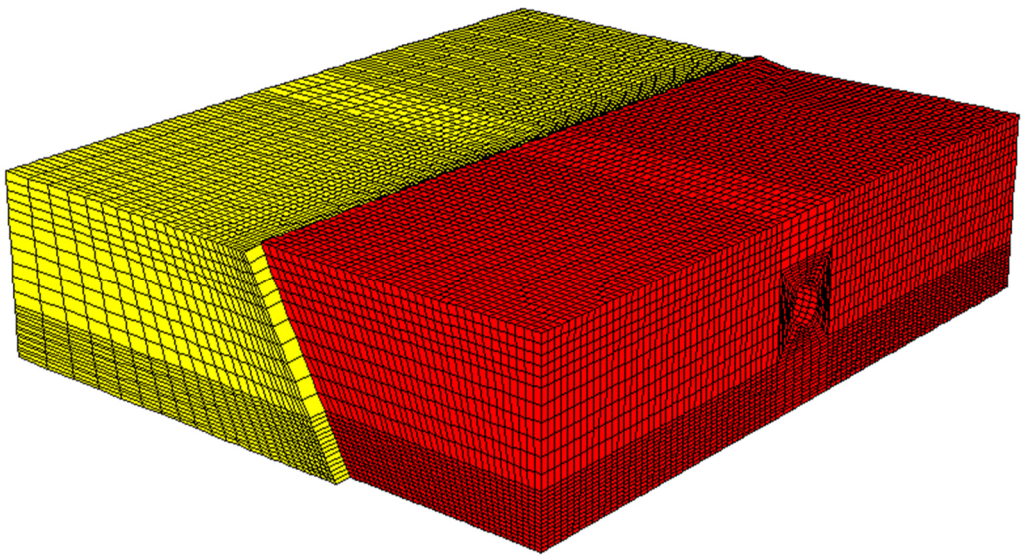

**Fig. 11**

a)

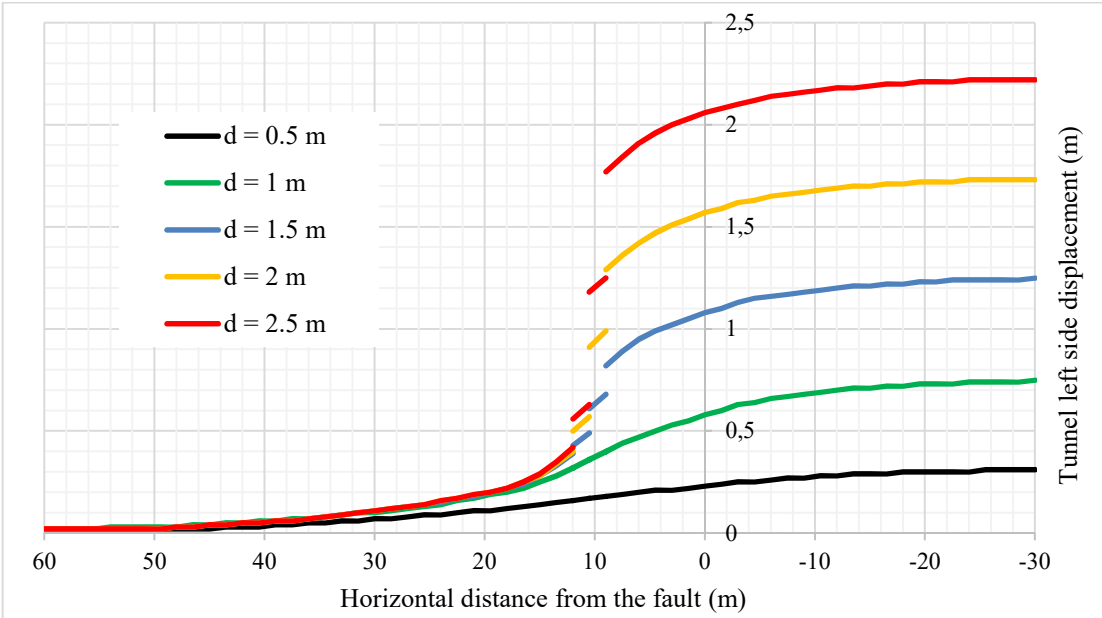
d = 0.5 m
d = 1 m
d = 1.5 m
d = 2 m
d = 2.5 m
2,5
2
1,5
1
0,5
0
60
50
40
30
20
10
0
-10
-20
-30
Horizontal distance from the fault (m)
Tunnel left side displacement (m)

b)

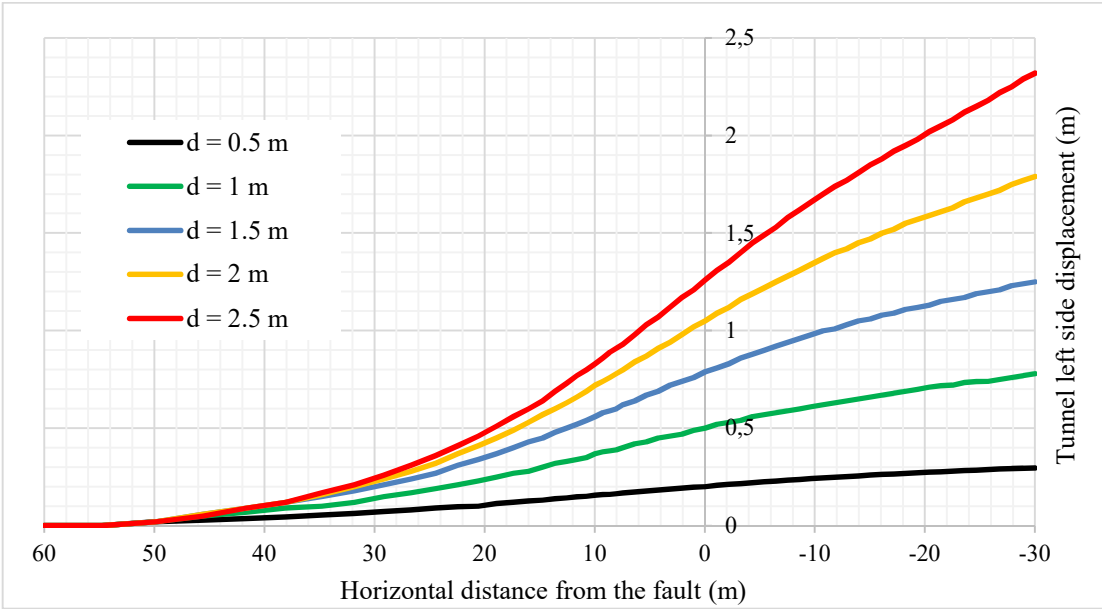
d = 0.5 m
d = 1 m
d = 1.5 m
d = 2 m
d = 2.5 m
2,5
2
1,5
1
0,5
0
60
50
40
30
20
10
0
-10
-20
-30
Horizontal distance from the fault (m)
Tunnel left side displacement (m)

**Fig. 12**

a)

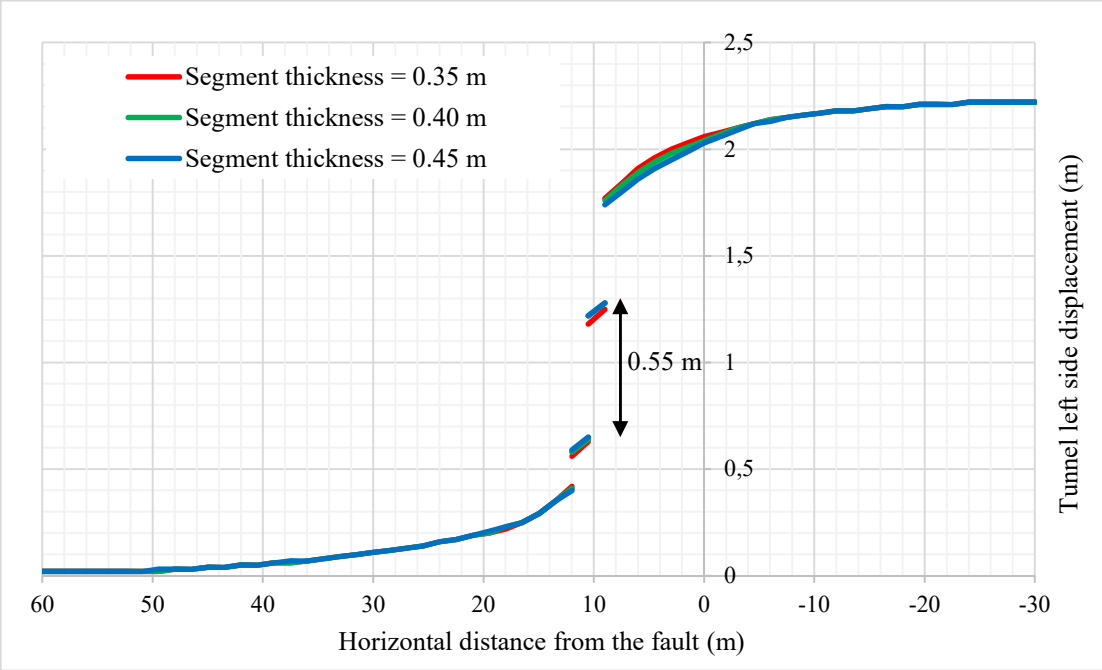
Segment thickness = 0.35 m
Segment thickness = 0.40 m
Segment thickness = 0.45 m
0.55 m
2,5
2
1,5
1
0,5
0
60
50
40
30
20
10
0
-10
-20
-30
Horizontal distance from the fault (m)
Tunnel left side displacement (m)

b)

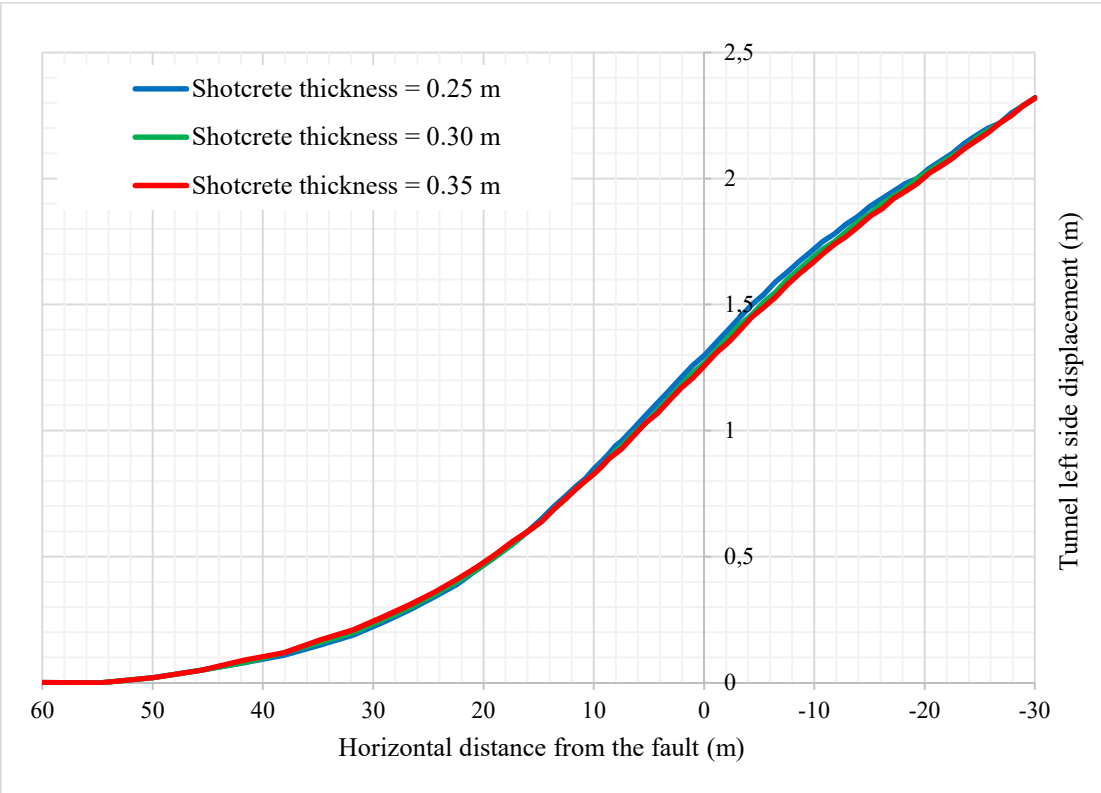
Shotcrete thickness = 0.25 m
Shotcrete thickness = 0.30 m
Shotcrete thickness = 0.35 m
2,5
2
1,5
1
0,5
0
60
50
40
30
20
10
0
-10
-20
-30
Horizontal distance from the fault (m)
Tunnel left side displacement (m)

**Fig. 13**

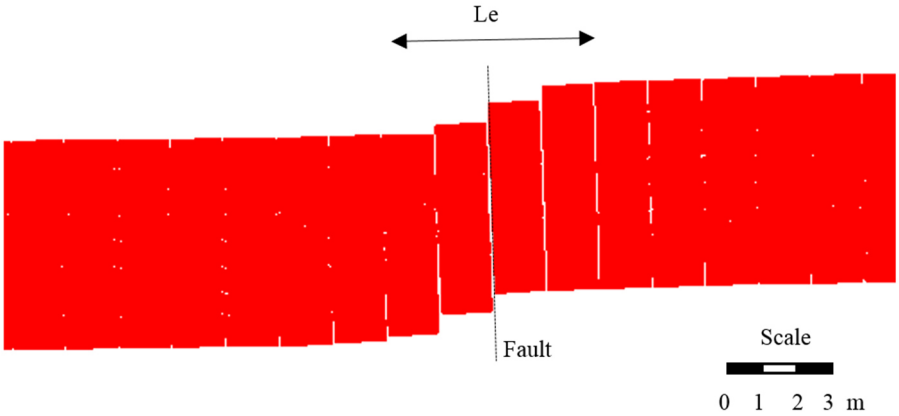


**Fig. 14**

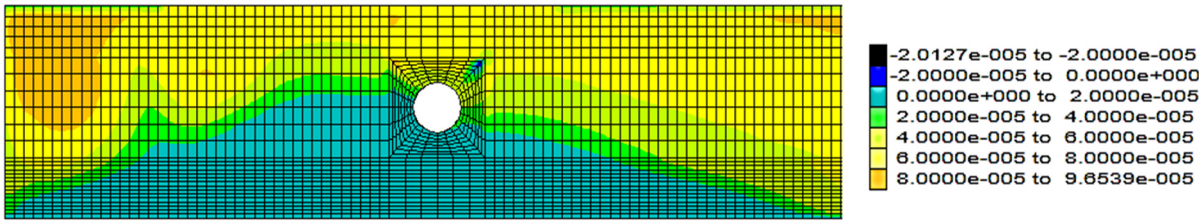


a. Segment thickness ($t_l$) = 0.35 m

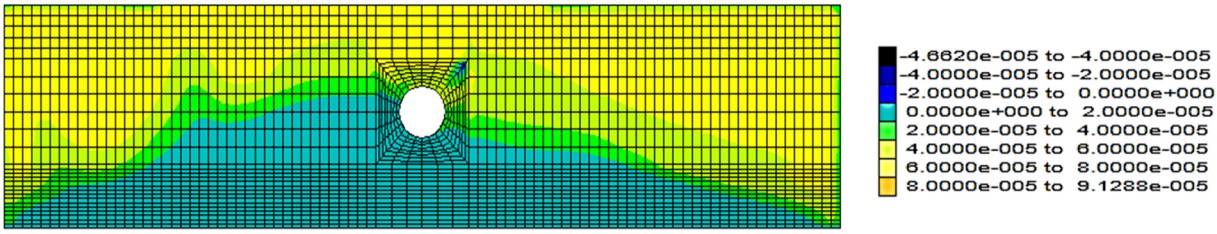


b. Segment thickness ($t_l$) = 0.45 m

**Fig. 15**

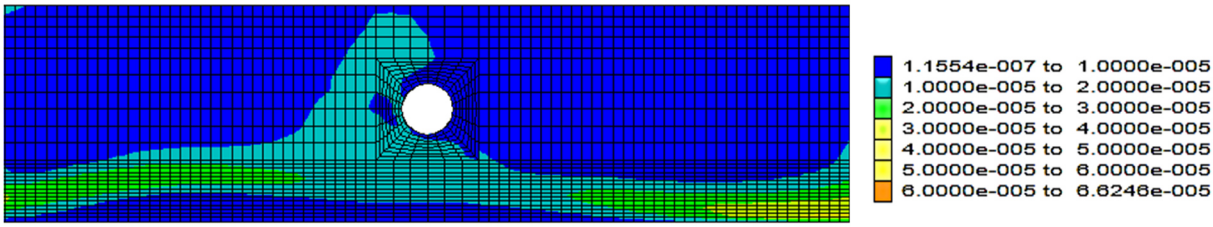


a. Shotcrete thickness ($t_l$) = 0.25 m

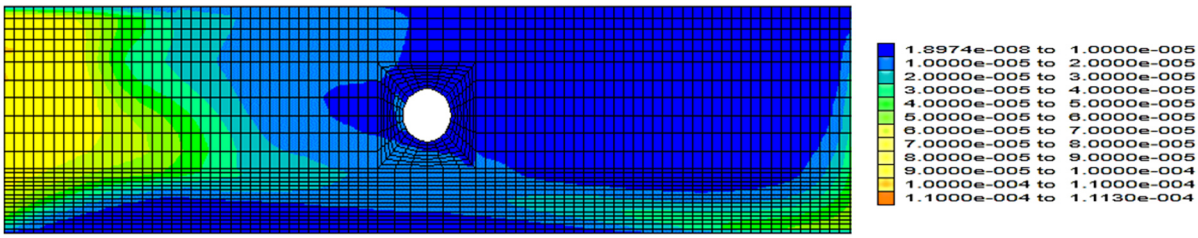


b. Shotcrete thickness ($t_l$) = 0.35 m

**Fig. 16**

a)

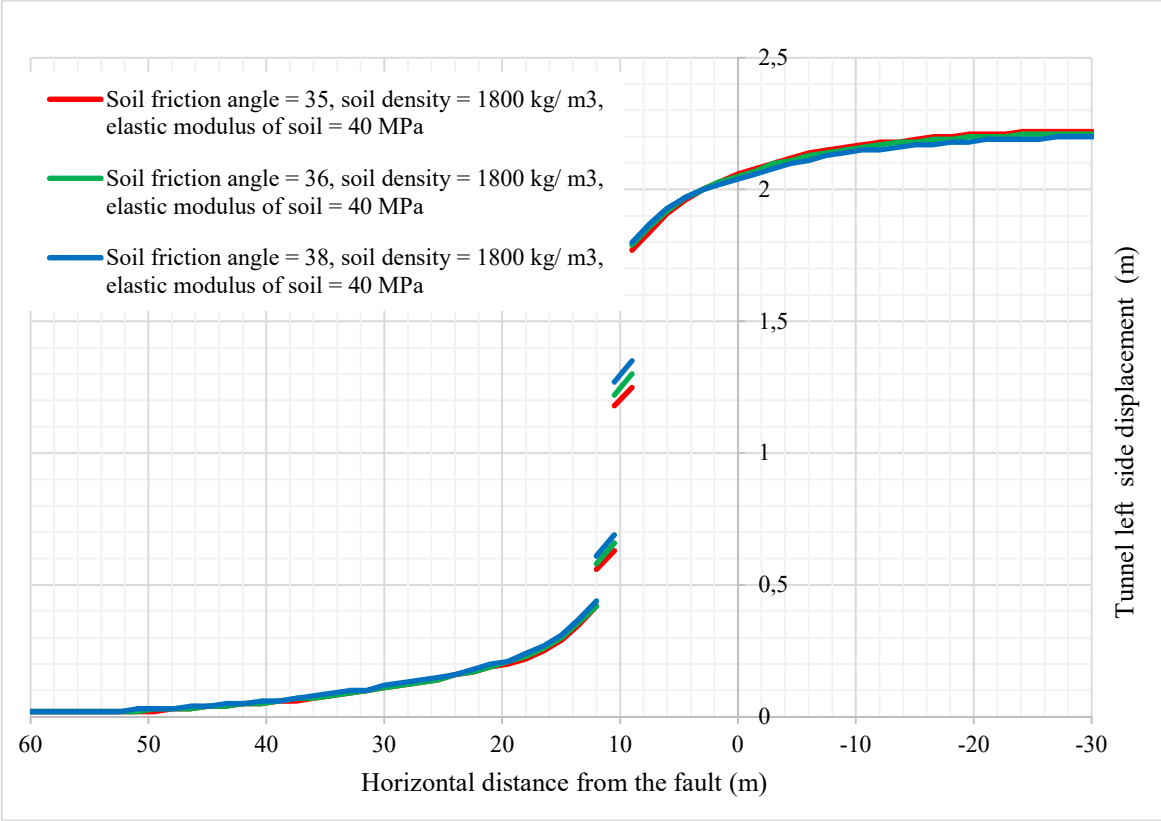
Soil friction angle = 35, soil density = 1800 kg/ m3, elastic modulus of soil = 40 MPa
Soil friction angle = 36, soil density = 1800 kg/ m3, elastic modulus of soil = 40 MPa
Soil friction angle = 38, soil density = 1800 kg/ m3, elastic modulus of soil = 40 MPa
2,5
2
1,5
1
0,5
0
60
50
40
30
20
10
0
-10
-20
-30
Horizontal distance from the fault (m)
Tunnel left side displacement (m)

b)

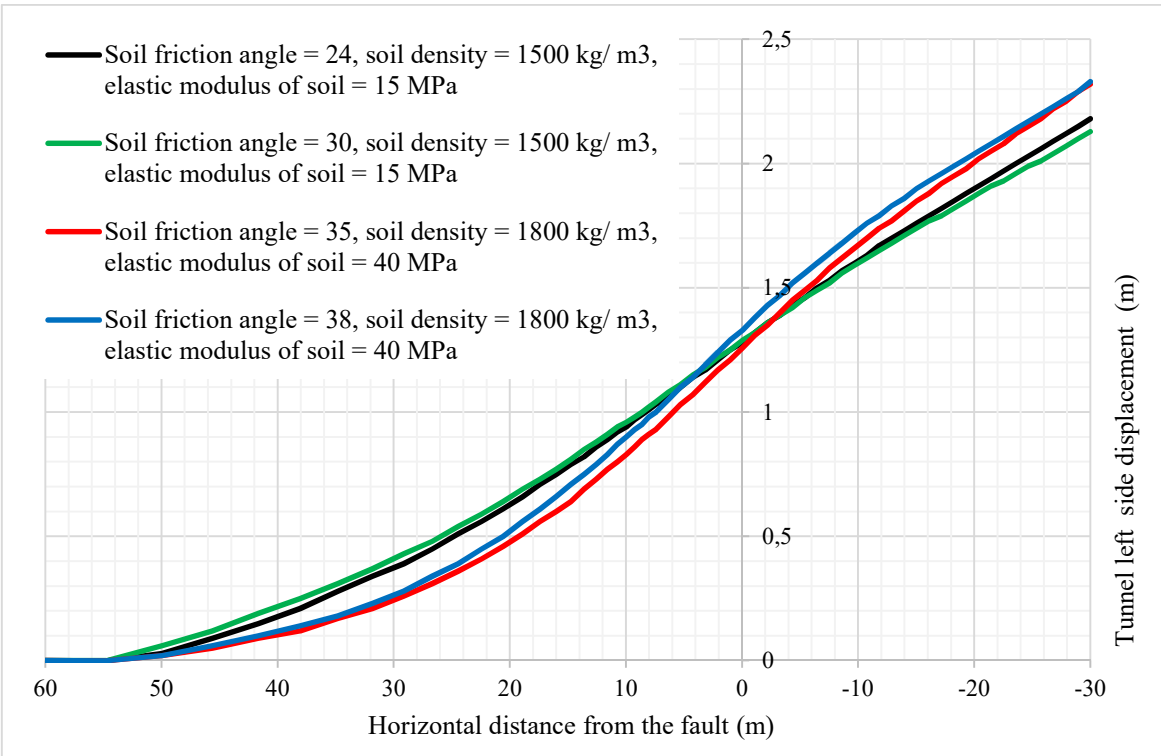
Soil friction angle = 24, soil density = 1500 kg/ m3, elastic modulus of soil = 15 MPa
Soil friction angle = 30, soil density = 1500 kg/ m3, elastic modulus of soil = 15 MPa
Soil friction angle = 35, soil density = 1800 kg/ m3, elastic modulus of soil = 40 MPa
Soil friction angle = 38, soil density = 1800 kg/ m3, elastic modulus of soil = 40 MPa
2,5
2
1,5
1
0,5
0
60
50
40
30
20
10
0
-10
-20
-30
Horizontal distance from the fault (m)
Tunnel left side displacement (m)

**Fig. 17**

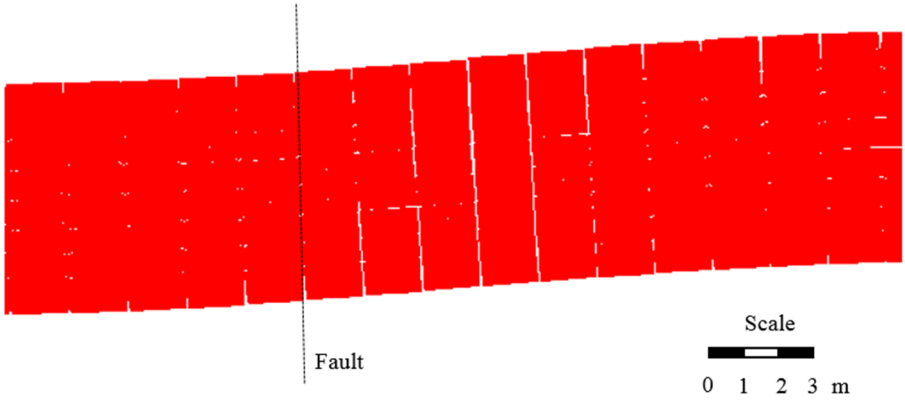


**Fig. 18**

a)

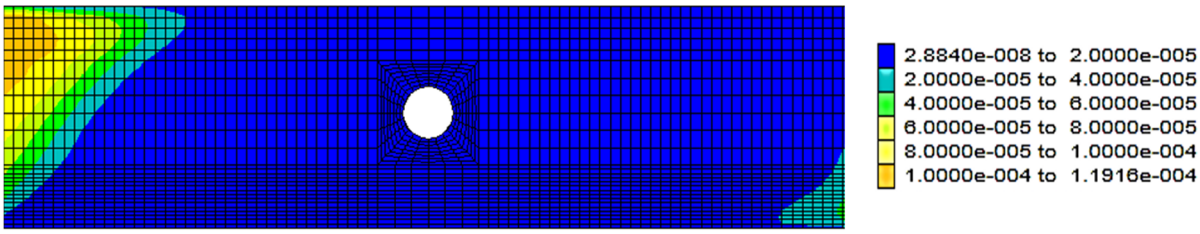


b)

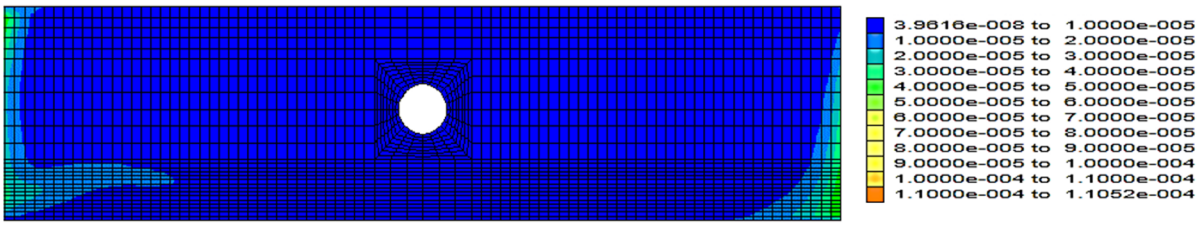


**Fig. 19**

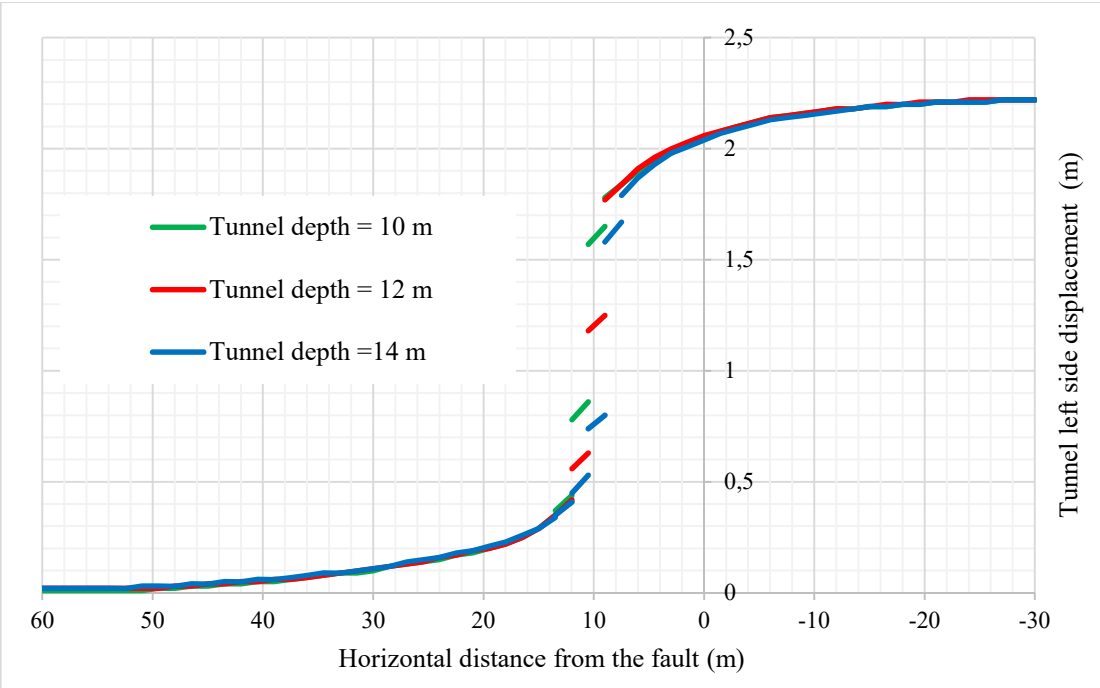


**Fig. 20**

a)

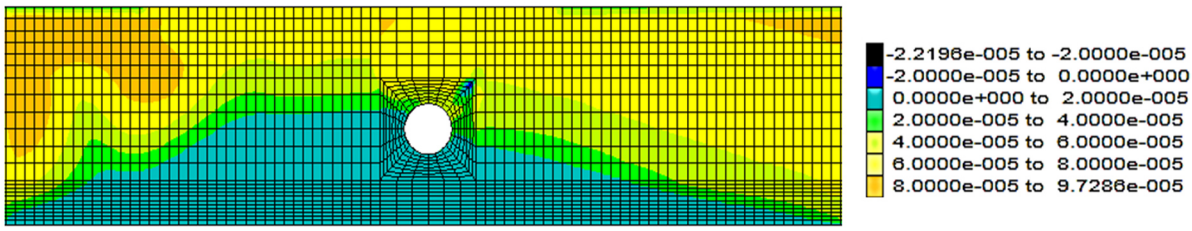


b)

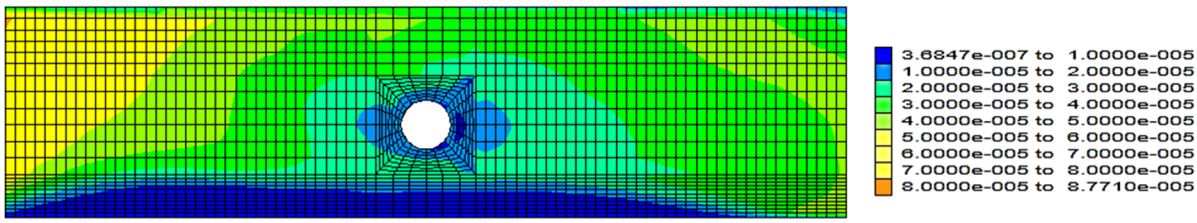


**Fig. 21**

a)

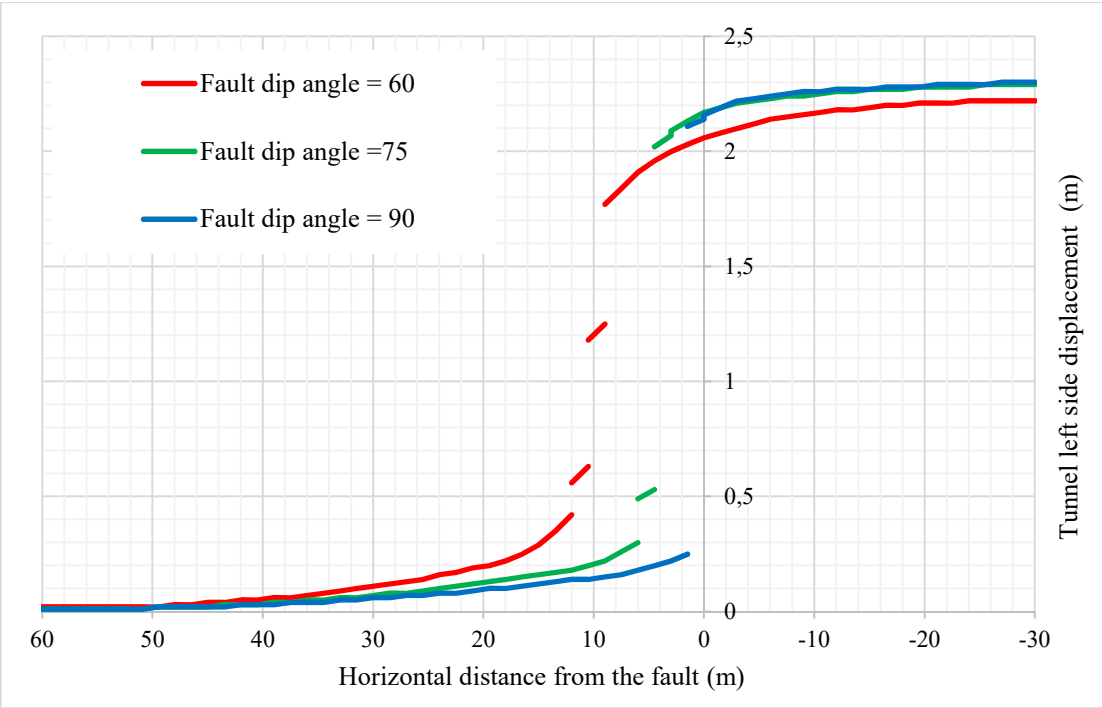
Fault dip angle = 60
Fault dip angle =75
Fault dip angle = 90
2,5
2
1,5
1
0,5
0
60
50
40
30
20
10
0
-10
-20
-30
Horizontal distance from the fault (m)
Tunnel left side displacement (m)

b)

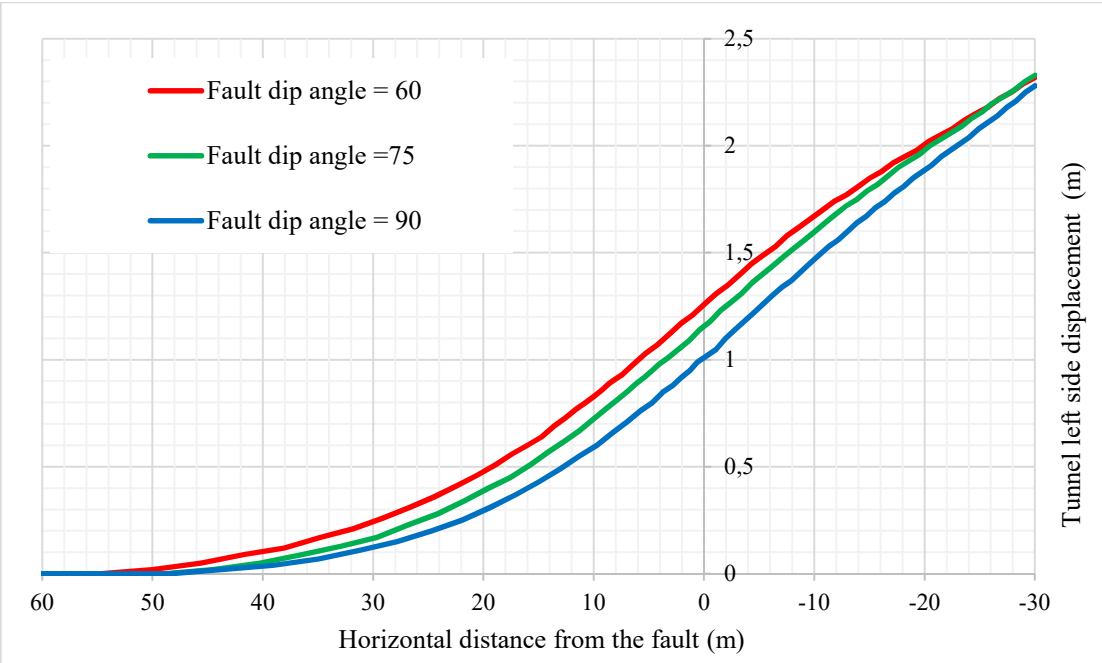
Fault dip angle = 60
Fault dip angle =75
Fault dip angle = 90
2,5
2
1,5
1
0,5
0
60
50
40
30
20
10
0
-10
-20
-30
Horizontal distance from the fault (m)
Tunnel left side displacement (m)

**Fig. 22**

a. Fault dip angle (α) = 75°

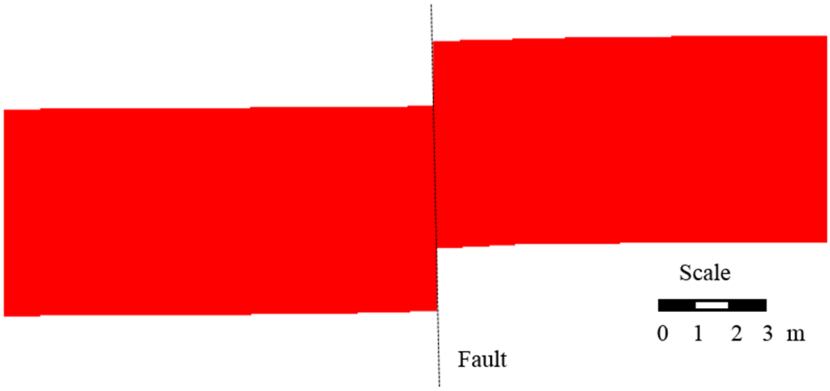


b. Fault dip angle (α) = 90°

**Fig. 23**

a)

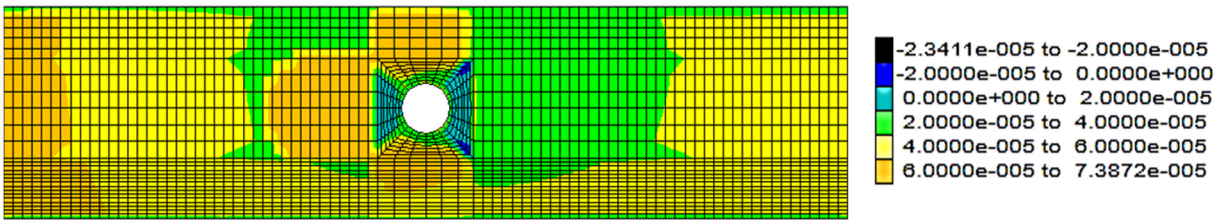


b)

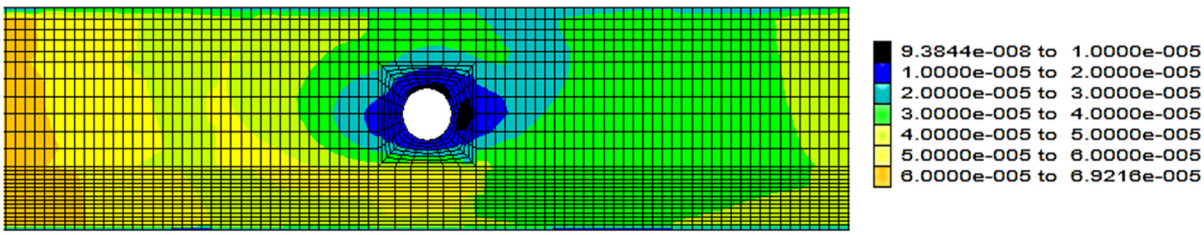


**Fig. 24**